8-10-2021 2:00 PM

Investigation of the Energy Source for an Early Dynamo in Vesta from Experiments on Electrical Resistivity of Liquid Fe-10wt%Ni at High Pressures

Eric M. Lenhart, *The University of Western Ontario*

Supervisor: Secco, Richard A., *The University of Western Ontario*
A thesis submitted in partial fulfillment of the requirements for the Master of Science degree in Geophysics
© Eric M. Lenhart 2021

Investigation of the Energy Source for an Early Dynamo in Vesta from Experiments on Electrical Resistivity of Liquid Fe-10wt%Ni at High Pressures

Abstract

Investigation of energy sources in an early dynamo in Vesta has been carried out using high pressure-temperature experimental studies. Electrical resistivity of Fe-10wt%Ni was measured at 2-5 GPa up to 2082 K in the liquid state and compared to previous results of pure Fe and pure Ni. Thermal conductivity was calculated from electrical resistivity to determine adiabatic core heat flux. The results are applied to determine whether thermal convection could be responsible for the putative dynamo in early Vesta's core. An adiabatic core heat flux of ~300 MW at the top of Vesta's core is estimated from this study and compared to a range of estimates of heat flux through the CMB of 1.5-78 GW. It is concluded that thermal convection would have occurred, playing an important role as an energy source of dynamo action that generated a magnetic field for tens of millions of years in Vesta's early history.

Keywords

Fe-10wt%Ni, Vesta, Resistivity, High-pressure, Thermal conductivity, Thermal convection, Dynamo energy sources, iron alloys

Summary for Lay Audience

The electrical resistivity of the metal core of a small, Earth-like asteroid body was experimentally studied using a sample with matching conditions of pressure, temperature, and composition. The electrical resistivity of the top of a body's core can tell us its thermal conductivity and therefore the rate at which heat passes via conduction through the outermost portion of the core. If the conducted heat is less than the total heat flowing out of the core into the mantle, then the missing heat is due to thermal convection of the liquid core. Convection of a liquid iron alloy has the potential to generate the magnetic fields observed on Earth and similar bodies, although heat transfer is not the only cause for convection.

In the experiments, the electrical resistivity of a small sample of an alloy of 90% iron and 10% nickel by weight (Fe10Ni) was measured at high temperatures (a few hundred Kelvin above melting) and high pressures. A 1000-ton cubic anvil press compressed a small sample wire inside a larger (~3.2 cm) cubic pressure cell to a target pressure in the range 2 to 5 GPa. Wires contacting each side of the Fe10Ni wire formed both thermocouples and electrodes on each end. The thermocouples measured temperature, while the electrodes completed a circuit, allowing voltage across the sample to be measured. These measurements gave the resistance of the sample, the electrical resistivity, and, by simple calculation, the thermal conductivity of Fe10Ni at specific temperatures and pressures.

The results are applied to the second-largest asteroid, Vesta. This asteroid, like Earth, is differentiated into a core, mantle, and crust. Meteorites known to have originated on Vesta show that early Vesta had a magnetic field generated internally. Thermal conductivity estimates of the alloy Fe10Ni from this study allow an estimate the amount of heat flow, 2 mW/m^2, conducted through the outermost region of Vesta's core early in its history. Because these results are lower than existing estimates of total heat flow from Vesta's core to its mantle, Vesta's core likely experienced thermal convection early in its history, which could have generated its magnetic field.

Co-Authorship Statement

Chapter 3, the body chapter of this thesis, is a manuscript currently under peer review for publication.

My contributions to this chapter included (1) construction of experimental components for the pressure cell, (2) performance of high pressure-temperature experiments in a 1000-ton cubic anvil press, (3) post-experiment sample macro-analyses (i.e. sample sectioning and microscopy), (4) data analysis and interpretation, and (5) writing and revising the chapter.

Dr. Richard A. Secco's contributions to the chapter included: (1) the concept for the project (2) financial support (3) discussions related to data interpretation and (4) feedback on the written manuscript.

Acknowledgments

Contents

List of Figures

List of Tables

List of Appendices

Glossary of Abbreviations Used

at%: atomic percentage

bcc: body-centered cubic

BSE: back-scattered electron

CMB: core mantle boundary

DFT: density functional theory

EMPA: electron microprobe analysis

fcc: face-centered cubic

hcp: hexagonal close-packed

HED: Howardite-Eucrite-Diogenite

ICB: inner core boundary

MD: molecular dynamics

wt%: weight percentage

Chapter 1

1   Introduction

The magnetosphere deflects harmful radiation from space making the Earth's magnetic field critical for the survival of life on Earth (e.g., Jones, 2015). To understand the dynamics of the interiors of planets including the processes that generate our magnetic field, one important method is the study of heat transfer. Near the top of the core, the amount and type of heat transfer remains uncertain. Once these outer core dynamics are better constrained, we can better understand internal dynamos and inner core formation.

The two possible types of heat transport in the liquid outer core are conduction and convection. The focus of the experimental part of this study is on thermal conduction while the implications for the study will be related to thermal convection. To calculate the conductive (i.e. adiabatic) heat flow at the top of the core, the thermal conductivity of materials comprising the region is needed. Thermal conductivity of metals and their alloys can be calculated from their measured electrical resistivity using the Wiedemann-Franz Law. The goal of this research is to experimentally measure the electrical resistance of liquid Fe-10wt%Ni (Fe10Ni) samples in order to draw conclusions about the style of heat flow in small differentiated bodies such as Vesta and the possibility of thermal convection as an energy source of internally generated magnetic fields in such bodies.

1.1   Heat Flow through Terrestrial Planetary Bodies

Terrestrial planetary bodies are defined by a silicate mantle and a metallic core; the core is often further divided into a liquid metallic outer core and a solid metallic inner core. Some non-planetary bodies, such as non-differentiated asteroids, are also termed "terrestrial" if they possess a silicate crust. The term "terrestrial planet" is often used to include any terrestrial body in hydrostatic equilibrium, regardless of orbital path and planetary status (e.g., Earth's moon), but for clarity, the term "terrestrial planetary body" will be used throughout this work to include both planets and satellites that are terrestrial-like in their bulk composition and in their differentiated state. Because most

seismological observations are of Earth, knowledge about Earth is often extrapolated to other terrestrial bodies when the data about them are limited. General information about the interiors of such bodies, such as bulk density and therefore composition, moment of inertia and therefore state of differentiation, can be constrained remotely by gravity measurements using Doppler tracking (e.g., Konopliv *et al*, 2011). Remote magnetometry provides critical information on the presence of a magnetic field which may provide important clues to core composition, physical state, and dynamics.

Several sources generate the heat that flows out through a planetary body. Because heat is a low-quality form of energy, heat originates by conversion from other types of energy that exist in the planet's interior. For example, since each planetary body formed through the accretion of smaller objects, the thermal energy derived from original kinetic energy and gravitational potential energy from the constituent aggregated parts has been exiting the planetary body as heat for billions of years. Additionally, the difference of density between silicates and metals in terrestrial planetary bodies has led to gravitational segregation: the gravitational potential energy of denser materials (metals) has caused them to sink toward the center of the planetary body, generating heat via friction along the way. As more material accretes and the pressure inside of a planet increases, heat is also generated due to adiabatic compression. As the inner core solidifies, some heat of crystallization is released. Currently, some heat also comes from radioactive decay of certain elements, such as K, U, and Th. In the early solar system, major sources of heat included ^{26}Al and ^{60}Fe.

According to thermodynamics, heat inside planetary bodies moves from areas of higher temperature to areas of lower temperature—i.e., from the core outward—via either convection or conduction. While convection can occur by more than one mechanism (see 1.3.2), thermal convection is the cyclical movement of materials due to density differences caused by heating and cooling in a gravitational field. For example, in the outer core, hot liquid metal rises and cools, then sinks back toward the inner core, where it is heated and rises again. Conduction, on the other hand, is the unidirectional transfer of heat directly through atomic contact within materials.

1.2   Heat Flow through Terrestrial Planetary Cores

While heat flow occurs from the center of the core all the way to the surface of a planetary body, the region of interest for this research is the top of the core of the planetary body, directly below the core-mantle boundary.

1.2.1   Estimating Convection and Conduction

When examining heat flow at the top of the core of a terrestrial planetary body, the focus is on estimates of three values: heat flow across the core-mantle boundary (CMB), total heat flow due to conduction at the top of the core, and total thermal convection in the liquid part of the core (see Figure 1.1). Heat flow across the CMB is useful as a constraint because there is no mass transfer across the CMB and therefore only one form of heat transfer: conduction. If all this heat flow across (or through) the CMB can be accounted for by conduction at the top of the core, then the heat flow at the top of the core is adiabatic. But if the heat flow across the CMB exceeds the total conduction at the top of the core, then the thermal gradient there is said to be super-adiabatic. In the super-adiabatic case, a mechanism of additional heat flow is required to accommodate the demands of heat flow across the CMB. This is generally assumed to be thermal convection in the liquid part of the outer core.
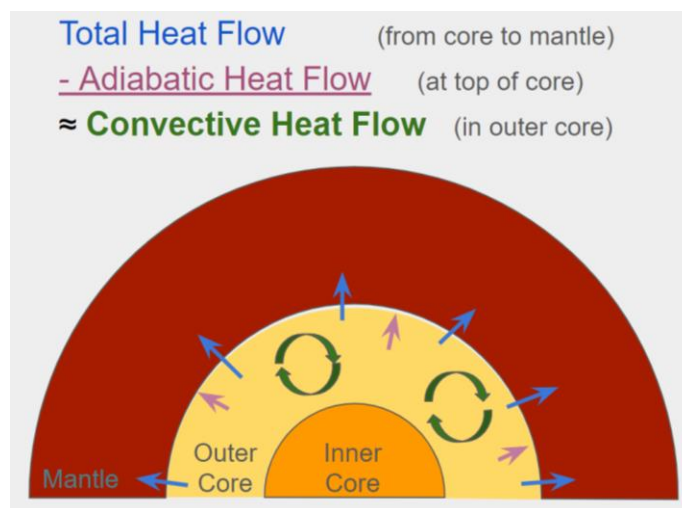
Figure 1.1: A schematic of heat flow near the core-mantle boundary of a generic differentiated terrestrial planetary body.

The heat flow through the CMB (which others have estimated based on factors such as temperature) is likely the sum of heat transfer due to conduction and any thermal convection; some of the heat brought by convection, however, could rest at the top of the core (Buffett, 2012). If all but one of these parameters are known, then the remaining one can be derived from the others. Specifically, heat due to convection is the most difficult to estimate directly using current methods. For this reason, this research seeks to use experimentation to estimate the thermal conductivity (κ) and conduction at the tops of planetary cores and—by using much needed estimates of the heat flow through the CMB—infer the core convective heat component.

Uncertainty remains about the precise value of heat flow across the CMB of each planet. For Earth, the uncertainty arises in part from estimates of the temperature on the core side of the CMB, ranging from 4000 K to 4500 K (Anzellini *et al.*, 2013), as well as the distribution of post-perovskite phase on the mantle side (Hirose *et al.*, 2015) which can provide estimates of temperature on the mantle side of the CMB. Currently, the heat flow across the core-mantle boundary of Earth is estimated to be at least 10 TW (Gomi *et al.*, 2013) and many have accepted a value of approximately 13.5 TW (Labrosse, 2015). In Mercury, heat flow through the CMB is thought to be super-adiabatic, which would imply current thermal convection in its outer core (Berrada *et al.*, 2021), but the weakness of Mercury's magnetic field seems to imply a more complicated thermal profile, such as a thermally stratified outer core (Wicht *et al.*, 2007). For Ganymede, thermal evolution models have estimated heat flux across the CMB to be ~1-3.3 mW/m^2 after 4.5 Gyr, which, for a core of radius 500 km, means a total heat flow across the CMB of ~30-100 GW (Hauck *et al.*, 2006).

1.2.2   Thermal Conductivity Calculation

One calculation central to this research is the estimation of thermal conductivity as a function of electrical resistivity. This is useful because electrical resistivity is much easier to measure than thermal conductivity. The equation used for the calculation, called the Wiedemann-Franz Law (Wiedemann and Franz, 1853), states that the thermal conductivity (κ) of a given material is inversely proportional to its electrical resistivity (ρ)

and directly proportional to the product of its temperature (T) and the Lorenz number (*L*), which has the theoretical value called the Sommerfeld value of $2.44 \times 10^{-8} \ W\Omega K^{-2}$:

$$\kappa = \frac{LT}{\rho} \qquad (\text{Eq. 1.1})$$

This means that the measured values of electrical resistivity of metal alloys at high pressures and temperatures can be used to find the thermal conductivity of those same metal alloys at the same conditions. This law is empirical and not accurate in all cases, in part because it accounts for only the electronic contributions to thermal conductivity but not for other factors such as atomic thermal vibrations which contribute a phonon conductivity (Watanabe *et al.*, 2019). However, in metals, electronic thermal conductivity generally overwhelms the phononic thermal conductivity (Klemens and Williams, 1986) and the Wiedemann-Franz Law is therefore a reasonable estimate of thermal conductivity.

Additionally, the electrical resistivity may be estimated at different pressures than those used in the experiment. At the melting temperature (T_M), the relationship between pressure (*P*) and electrical resistivity (ρ) is given by (Stacey and Anderson, 2001):

$$\left(\frac{\partial ln\rho}{\partial P}\right)_{T_M} = 0 \quad (\text{Eq. 1.2})$$

This means that the electrical resistivity of a metal is constant along the melting boundary regardless of pressure. Intuitively, this seems to be possible since the melting boundary increases in temperature, which is accompanied by increase in resistivity, as pressure increases, which is accompanied by decrease in resistivity. The antagonistic effects of pressure and temperature on resistivity may therefore offset each other along the pressure dependent melting boundary. If validated, this relationship would allow for measurements made at lower pressures relative to the core to be reasonably extrapolated to higher pressures, such as those at the top of the core of Earth.

1.2.3   Composition of Earth's Core as an Analogue of Vesta's Core

Estimating the conductive heat flow in any region requires knowledge of the region's composition. While this study focuses on application of results to asteroid (4) Vesta—a differentiated terrestrial-like planetary body—much of what is known about the interiors of terrestrial planetary bodies comes from our detailed knowledge of Earth's interior. Due to evidence such as seismological density profiles and the siderophile content in iron meteorites (e.g., Jones and Drake, 1983), we know that the liquid outer cores of terrestrial planetary bodies are comprised primarily of Fe and secondarily of Ni—in Earth, 5-10wt%Ni (e.g. Poirier, 1994). Additionally, various evidence, such as seismological estimates of density, indicates that lighter elements are also present in the Earth's core. In particular, Si, O, S, H, C, and Mg are each thought to be candidates, either alone or in some combination. The exact proportion of each of these light elements is not well-constrained, but among these, Si, S and O are thought to be dominant (e.g., Hirose *et al*., 2017; Takafuji *et al.*, 2015)

1.3   Applications to Heat Flow in the Cores of Terrestrial Planetary Bodies

1.3.1   Inner Core Age

The solid inner core of planetary bodies forms as secular cooling of the liquid outer core causes it to cross the pressure dependent melting boundary of the core liquid. Pure Fe freezes out and by gravitational settling, is thought to have incrementally formed Earth's solid inner core (e.g. Nimmo, 2015). Since pressures are greatest in the center of a body, this mode of inner core solidification proceeds upward from the bottom (i.e. center) of the core. Heat flow out of the core, therefore, may tell us when Fe began to solidify, which corresponds to the age of the inner core. Models that estimate this age are dependent on the thermal conductivity of the liquid outer core. A higher κ implies a more rapid secular core cooling, which implies a later formation of the inner core (e.g. Gomi *et al.*, 2013). However, the cores of small differentiated bodies, such as some asteroids, may form in an entirely different way than the Earth's inner core formed. Instead of bottom upward

solidification, small differentiated bodies may form a solid inner core from the top downward (e.g., Neufeld, 2019; Williams, 2009).

Based on observations of heat flow at the top of Earth's core, various researchers have estimated the age of Earth's solid inner core as ~1$\pm$0.5 billion years. For example, models of Earth's outer core as an Fe-Si-O-S mixture, taking into account gravitational segregation as well as seismological and mineralogical data, have led to estimates of the maximum age of Earth's inner core at 0.6 billion years old (Davies, 2015). However, this number increases to as high as 1.5 billion years in the same models if the thermal gradient at the top of the core is taken to be sub-adiabatic currently rather than super-adiabatic. More accurate models of heat flow through the top of the core, therefore, are crucial to these estimates. High-pressure experimental studies that considered light elements and resistivity saturation (described in 2.1.1) result in an inner core age estimate of 0.7 billion years (Labrosse, 2015).

1.3.2 The Internal Generation of Magnetic Fields

The most important application of this research is a better understanding of the mechanism powering the dynamos of terrestrial planetary bodies. The likeliest energy source responsible for each of the past and present magnetic fields of terrestrial planetary bodies is, in most cases, some form of convection. The convective movement of electrical charge in Earth's liquid outer core, likely in helical columns (Taylor columns) roughly parallel with the Earth's axis of rotation (Roberts, 1968; Busse, 1970), cause a dynamo effect, which generates a magnetic field (Larmor, 1919). Thermal convection may be thought of as the process of converting thermal energy into kinetic energy, while the dynamo effect may be thought of as the means of converting some of this kinetic energy into electromagnetic energy.

Two modes of convection that likely play a role in the liquid outer core of a planetary body are thermal convection, described in 1.2, and compositional (or chemical) convection. Compositional convection occurs as the inner core freezes and pure Fe settles onto the solid inner core and leaves a locally higher concentration of light elements above the inner core boundary (ICB). The change in density of the liquid just above the ICB

generates a churning motion powered by buoyant forces in the liquid. If the solidified matter is less dense than the outer core overall, it rises toward the CMB; if it is denser than the liquid, it sinks. This latter case for Fe gradually formed Earth's solid inner core and may drive the geodynamo today (Braginsky, 1963; Loper, 1978). The freezing of other compounds such as magnesium oxide (O'Rourke and Stevenson, 2016) or silicon dioxide (Hirose *et al.,* 2017) in a top down scenario have also been suggested as power sources of convection in the outer core at earlier stages of Earth's development, as the strength of each type of convection may vary throughout a planetary body's history. In general, the thermal convection inside a planetary body will decrease over time after formation as internal heat leaves the planetary body. The thickness of the mantle can also influence dynamo generation in the core, with thinner mantles reducing the likelihood of dynamo generation (Freitas *et al.*, 2021). This is due to the control a planetary body's mantle has over heat flow out of the core (Olson, 2016); the amount of heat the mantle draws from the outer core (along with the magnitude of core conductive heat flow) dictates whether or not thermal convection in the outer core occurs.

The historical strength and direction of a magnetic field can be inferred from paleomagnetic records, but understanding heat flow in the core indicates *how* the planetary body's magnetic field was generated at various times throughout its history. For Earth, the geomagnetic field is recorded as far back as 3.5 billion years ago (Tarduno *et al.*, 2010). The Earth's field has likely always been primarily formed by an internal dynamo, but an unanswered question is whether this dynamo is and has been driven by thermal convection or chemical convection or some combination of both with varying contributions of each throughout the life of the dynamo. By constraining the value of conductive heat flow (from thermal conductivity values) at the top of a given core, this research aims to determine if thermal convection in the outer core was possible, which will help to identify if thermal convection could have been a source of the magnetic field of a small differentiated object such as early Vesta.

1.4   Asteroid (4) Vesta

The application of the data in this study is to the asteroid (4) Vesta. As the fourth asteroid discovered, Vesta is the second-largest asteroid and the brightest asteroid as viewed from

Earth, faintly visible to the naked eye at times. The Howardite-Eucrite-Diogenite (HED) clan of meteorites is widely recognized to likely have originated from Vesta (McCord *et al.*, 1970; Consolmagno and Drake, 1977). HED meteorites and remote sensing techniques provide us most of the data we have relevant to Vesta's history.

The thermal history of Vesta likely began soon after the injection of ^{26}Al into the solar system, which rapidly decayed and heated early Vesta (e.g., Weisfeiler *et al*., 2016). This likely resulted in a global magma ocean (Righter and Drake, 1997; Mandler and Elkins-Tanton, 2013) and, eventually, the differentiation of Vesta into a metal core, a silicate mantle, and a basaltic crust. W isotopes in HED meteorites show that this differentiation happened 4564.1 ±1.7 million years ago, which is soon after Vesta's formation (Kleine *et al.,* 2004). Weisfeiler *et al*. (2016) suggest that an important cooling mechanism of Vesta was crustal foundering, in which the cooled solid on the surface of a lava lake or ocean is covered by the less dense liquid.

While not one of the HED meteorites is predominantly iron, these meteorites can still inform us about the metallic interior of Vesta. The partitioning of P and La in eucrites was an early indicator that the parent body, Vesta, had formed a metallic core (Newsom and Drake, 1983). More recently, natural remanent magnetization of eucrite ALHA81001 has shown that Vesta once possessed an internally generated dynamo (Fu *et al.*, 2012), presumably in a liquid iron core.

Additionally, iron meteorites recovered on Earth can provide us with insight into Vesta's interior. Evidence in iron meteorites such as Widmanstätten morphologies can tell us about the cooling rate of the metal as it crystallized (e.g., Goldstein *et al*., 2009). While we have no samples from Vesta's interior, we do have a broad sampling of iron meteorites to help us make informed estimates of cooling rates (Weiss *et al.*, 2010). Such cooling rate estimates, especially if there is evidence to suggest they were clad with a silicate layer, could inform us about heat flow out of the core into the mantle. All iron meteorites have 4wt% Ni or greater, which guides the choice of the Fe-Ni composition used in this experimental study.

Vesta was first visited by the *Dawn* mission in 2011. Gravity measurements confirmed that the asteroid is differentiated, with a metallic core of about 110 km in radius. Vesta also possesses a large southern basin, Rheasilvia. The impact responsible for this basin would have been sufficiently large to generate the Vesta-family of asteroids observed (Russell *et al.*, 2012). While these basins indicate clearly that Vesta is not in hydrostatic equilibrium and therefore not a dwarf planet, Vesta's differentiated core makes it applicable to this study.

1.5   Aim of this Research

The primary objective of this research is to understand if a thermal convection energy source contributed to the dynamo that produced the magnetic field in early Vesta. Experimentally, to reach this objective, the electrical resistivity of a liquid alloy of 90wt% Fe and 10wt% Ni (Fe10Ni) was measured at simultaneous temperatures up to 2100 K and pressures up to 5 GPa using a 1000-ton cubic anvil press. Using these measurements, thermal conductivity of the sample material will be estimated. Then, those results and the principles of thermodynamics will be used to estimate the amount of adiabatic heat flow at the top of the core of asteroid Vesta.

With these estimates of adiabatic heat flow at the top of Vesta's core, further applications are possible with the help of other heat flow estimates. If existing estimates of heat flow at the CMB of early Vesta are greater than the estimates of adiabatic heat flow at the top of the core of early Vesta obtained in this study, this allows an interpretation that thermal convection occurred in its core. This knowledge will advance our understanding of the internal dynamos that generate planetary body magnetic fields. Since Vesta has no internally generated magnetic field presently, the application is most relevant to the earliest stages of its history when heat flow was much greater and when the HED meteorite record shows an internally generated magnetic field (Fu *et al.*, 2012).

References

Berrada, M., Secco, R.A., Yong, W. 2018. Decreasing electrical resistivity of gold along the melting boundary up to 5 GPa. *High Pressure Research*. 38: 367-376.

Braginsky, S.I. 1963. Structure of the F layer and reasons for convection in Earth's core. *Dokl. Akad. Nauk. SSSR English Translation.* 149: 1311-1314.

Buffett, B. 2012. Geomagnetism under scrutiny. *Nature*. 485: 319-320.

Busse, F. 1970. Thermal instabilities in rapidly rotating systems. *Journal of Fluid Mechanics.* 44: 441-460.

Davies, C.J. 2015. Cooling history of Earth's core with high thermal conductivity. *Phys. Earth Planet. Inter.* 247: 65-79.

Freitas, D., Monteux, J., Andrault, D., Manthilake, G., Mathieu, A., Schiavi, F., Cluzel, N. 2021. Thermal conductivities of solid and molten silicates: Implications for dynamos in mercury-like proto-planets. *Physics of the Earth and Planetary Interiors*. 312: 106655.

Fu, R.R., Weiss, B.P., Shuster, D.L., Gattacceca, J., Grove, T.L., Suavet, C., Lima, E.A., Luyao, L., Kuan, A.T. 2012. An Ancient Core Dynamo in Ancient Vesta. *Science*. 338: 238-241.

Goldstein, J.I., Scott, E.R.D., Chabot, N.L. 2009. Iron meteorites: Crystallization, thermal history, parent bodies, and origin. *Chemie der Erde*. 69: 293-325.

Gomi, H., Ohta, K., Hirose, K., Labrosse, S., Caracas, R., Verstraete, M.J., Hernlund, J.W. 2013. The high conductivity of iron and thermal evolution of the Earth's core. *Physics of the Earth and Planetary Interiors.* 224: 88-103.

Hauck, S.A., Aurnou, J.M., Dombard, A.J. 2006. Sulfur's impact on core evolution and magnetic field generation on Ganymede. *Journal of Geophysical Research: Planets*. 111: E09008.

Hirose, K., Wentzcovitch, R., Yuen, D., Lay, T. 2015. Mineralogy of the deep mantle—The post-perovskite phase and its geophysical significance. *Treatise on Geophysics*. Elsevier, Oxford: 85-115.

Hirose, K., Morard, G., Sinmyo, R., Umemoto, K., Hernlund, J., Heffrich, G., Labrosse, S. 2017. Crystallization of silicon dioxide and compositional evolution of the Earth's core. *Nature*. 543: 99-101.

Jones, C. A. 2015. Thermal and Composition Convection in the Outer Core. *Treatise on Geophysics*. 2: 116-155.

Jones, J. H., and Drake, M. J. 1983. Experimental investigations of trace element fractionation in iron meteorites, II: The influence of sulfur. *Geochimica et Cosmochimica Acta*. 47: 1199-1209.

Kleine, T., Mezger, K., Munker, C., Palme, H., Bischoff, A. 2004. 182Hf-182W isotope systematics of chondrites, eucrites, and martian meteorites: Chronology of core formation and early mantle differentiation in Vesta and Mars. *Geochimica et Cosmochimica Acta*. 68, 2935-2946.

Klemens, P.G. and Williams, R.K. 1986. Thermal conductivity of metals and alloys. *International Metals Reviews*. 31, 197-215.

Labrosse, S. 2015. Thermal Evolution of the Core with a High Thermal Conductivity. *Physics of the Earth and Planetary Interiors*. 247: 36-55.

Larmor, J. 1919. Possible rotational origin of magnetic fields of sun and earth. *Electrical Review*. 85: 412ff.

Loper, D.E. 1978. The Gravitationally Powered Dynamo. *Geophysical Journal International*. 54: 389–404.

Newsom, H.E. and Drake, M.J. 1983. Experimental investigation of the partitioning of phosphorus between metal and silicate phases: implications for the Earth, Moon and Eucrite Parent Body. *Geochimica and Cosmochimica Acta*. 47: 93-100.

Neufeld, J.A., Bryson, J.F.J., Nimmo, F. 2019. The Top-Down Solidification of Iron Asteroids Driving Dynamo Evolution. *Journal of Geophysical Research: Planets*. 124: 1331-1356.

Nimmo, F. 2015. Energetics of the Core. *Treatise on Geophysics*. 2: 27-55.

Olson, P. 2016. Mantle control of the geodynamo: Consequences of top-down regulation. *Geochemistry, Geophysics, Geosystems*. 17: 1935-1956.

O'Rourke, J.G., and Stevenson, D.J. 2016. Powering Earth's core with magnesium precipitation from the core. *Nature.* 529: 387-389.

Poirier, J.-P. 1994. Light elements in the Earth's outer core: A critical review. *Physics of the Earth and Planetary Interiors*. 85: 319-337.

Roberts, P.H. 1968. On the thermal instability of a rotating-fluid sphere containing sources. *Philosophical transactions of the Royal Society London.* 263: 93-117.

Russell, C.T., Raymond, C.A., Coradini, A., McSween, H.Y., Zuber, M.T., Nathues, A., De Sanctis, M.C., Jaumann, R., Konopliv, A.S., Preusker, F., Asmar, S.W., Park, R.S., Gaskell, R., Keller, H.U., Mottola, S., Roatsch, T., Scully, J.E.C., Smith, D.E., Tricarico, P., Toplis, M.J., Christensen, U.R., Feldman, W.C., Lawrence, D.J., McCoy, T.J., Prettyman, T.H., Reedy, R.C., Sykes, M.E., Titus, T.N. 2012. Dawn at Vesta: Testing the Protoplanetary Paradigm. *Science.* 336: 684-686.

Stacey, F., and Anderson, O. 2001. Electrical and thermal conductivities of Fe-Ni-Si alloy under core conditions. *Physics of the Earth and Planetary Interiors.* 124: 153–162.

Takafuji, N., Hirose, K., Mitome, M., Bando, Y. 2015. Solubilities of O and Si in liquid iron in equilibrium with $(Mg,Fe)SiO_3$ perovskite and the light elements in the core. *Geophysical Research Letters.* 32: L06313.

Tarduno, J.A., Cottrell, R.D., Watkeys, M.K., Hofmann, A., Doubrovine, P.V., Mamajek, E.E., Liu, D., Sibeck, D.G., Neukirch, L.P., Usui, Y. 2010. Geodynamo, Solar Wind, and Magnetopause 3.45 to 3.4 Billion Years Ago. *Science*. 327: 1238-1240.

Watanabe, M., Adachi, M., Uchikoshi, M., Fukuyama, H. 2019. Thermal Conductivities of Fe-Ni Melts Measured by Non-contact Laser Modulation Calorimetry. *Metallurgical and Materials Transactions*. 50: 3295-3300.

Weisfeiler, M., Turcotte, D.L., Kellogg, L.H. 2016. Modeling the early evolution of Vesta. *Meteoritics and Planetary Science*. 52: 859-868.

Weiss, B.P., Gattacceca, J., Stanley, S., Rochette, P., Christensen, U.R. 2010. Paleomagnetic Records of Meteorites and Early Planetesimal Differentiation. *Space Science Reviews*. 152: 341-390.

Wicht, J., Mandea, M., Takahashi, F., Christensen, U.R., Matsushima, M., Langlais, B. 2007. The Origin of Mercury's Internal Magnetic Field. *Space Science Reviews*. 132: 261-290.

Wiedemann, D., and Franz, R. 1853. Uber die Warme-Leitungfahligkeit der Metalle. *Annals of Physics and Chemistry*. 89: 497-531.

Williams, Q. 2009. Bottom-up versus top-down solidification of the cores of small solar system bodies: Constraints on paradoxical cores. *Earth and Planetary Science Letters*. 284: 564-569.

Chapter 2

2   Review of Relevant Research on Fe Alloys at High Pressures and Temperatures

Our knowledge about heat flow in metal alloys at the top of the cores of terrestrial planetary bodies comes through both experimental and theoretical approaches. Historically, research on planetary interiors using high-pressure methods began with a focus on the mantle (see review by Ito, 2015), such as the phase transition of spinel at around 410 km. To draw conclusions about the cores of planetary bodies instead, as this study does, the experimental approach involves high pressure experimentation on alloys of Fe. In many of these cases, the electrical resistivity is the quantity measured (from which thermal conductivity is easily estimated [see 1.3.2]). Additionally, theoretical approaches, which have focused on molecular-level models such as density functional theory, are also needed.

2.1 Experimental Results

An important method of estimating electrical resistivity at the top of the liquid outer core of terrestrial planetary bodies is high-pressure experimentation. These experiments are performed on small samples of Fe alloys using equipment such as a 3000-ton multi-anvil press (e.g. Silber *et al*. 2019) or a diamond anvil cell (e.g. Anzellini *et al.*, 2013; Gomi and Hirose, 2015), and usually record data with respect to three variables: pressure, temperature, and electrical resistivity. All the studies discussed here reached at least 8 GPa, with some reaching well over 100 GPa. All these studies, therefore, may be applied to the top of the core of a small terrestrial planetary body of the chosen composition and temperature; the experiments at the highest pressures may apply to Earth's core.

2.1.1   Iron

The most fundamental material to examine at outer core conditions is pure liquid Fe. Electrical resistivity measurements of Fe are crucial because a high electrical resistivity at the top of the core in turn implies a lower thermal conductivity there. This means less heat is conducted and therefore, depending on the heat flow through the core mantle

boundary (CMB), there may be thermal convection. The opposite is true of a low electrical resistivity. The electrical resistivity (ρ) of Fe has been shown to decrease with increasing pressure and increase with increasing temperature (T) (e.g., Secco and Schloessin, 1989; Silber *et al.*, 2018; Yong *et al.,* 2019). Recent studies on both liquid and solid Fe have shown that electrical resistivity does not change along the melting boundary above the 5 GPa triple point (Silber *et al.*, 2018; Yong *et al.*, 2019). One application of high-pressure resistivity experiments on pure Fe has been to constrain the heat conducted at the outermost core of Mercury (Deng *et al.*, 2013; Silber *et al.,* 2018) as well as the Moon, Mars, and Ganymede (Silber *et al.,* 2018).

At higher temperatures and pressures, Fe sometimes behaves differently than at lower temperatures and pressures. At temperatures near 4000 K, the resistivity of Fe is lower than extrapolations from lower temperature experiments or from prediction with the Bloch-Gruneisen equation, which suggests a strong resistivity saturation effect at such high temperatures (Ohta *et al.*, 2016). However, the interpretation of resistivity saturation may have instead been an effect of experimental artifact related to incorrect positioning of laser heating and possibly due to other experimental techniques such as the pseudo-four probe method (Zhang *et al.*, 2020). Theoretically, a saturation of resistivity is predicted to occur when the electron mean free path is about the same as the interatomic spacing (Ioffe and Regel, 1960). This criterion for resistivity saturation can be induced by static properties, such as impurities, or dynamic properties, such as changes in temperature or pressure (e.g., Kiarasi and Secco, 2015).

2.1.2   Nickel

High-pressure electrical resistivity experiments have also been performed on pure Ni (Silber *et al.*, 2017). The electronic structure of Ni and Fe are comparable since each element has an unfilled 3d shell so their electrical resistivities may be expected to behave similarly at high pressures. The electrical resistivity of Ni is also invariant along the melting boundary (Silber *et al.*, 2017). This result also extends Stacey and Anderson's (2001) prediction (see 1.2.2) to include Ni, even though it has an unfilled d-band.

2.1.3 Iron-Nickel Alloys

For this research, the most relevant experiments are those performed on liquid Fe-Ni alloys. Fe-10wt%Ni, the composition of this study, was studied at high pressures and temperatures by Huang *et al.* (1988). However, the temperature reached was less than 900 K. Lin *et al*. (2002) later performed similar studies up to 2382 K and 86 GPa. Both these studies provided data about the temperatures and pressures of structural phase transitions, but neither measured electrical resistivity. Kuznetsov *et al.* (2007) measured and described the electrical resistance of several Fe-Ni samples, including 10wt%Ni, up to 18 GPa but only up to 425 K.

High-pressure resistivity experiments on Fe alloyed with small amounts of Ni show differing effects on resistivity depending on temperature. At the pressure range of this study, studies on Fe-10wt%Ni have shown that near ambient temperatures, the presence of Ni increases resistivity by a large factor (~2.5) relative to pure Fe at the same temperature (Pommier, 2020); however, this effect is greatly reduced before temperatures near melting are reached. Similarly, at ambient temperatures and 60 GPa, the effect of 5at% Ni is experimentally shown to double the resistivity of Fe. However, at high temperatures and pressures, such as those at the CMB, the effect of Ni is predicted to be much more minor, with the modeled resistivity of Fe-10wt%Ni only about 15% greater than that of pure Fe (Gomi and Hirose, 2015). Such a pattern might be expected in this study as well, although pressures are much lower.

Studies have also been performed on the approximate complement: Fe-90at%Ni. At ambient pressures, the electrical resistivity of Fe-90at%Ni as a function of temperature has been measured (Kita and Morita, 1984), with the resistivity of ~120 $\mu\Omega\cdot$cm at melting temperatures, which is near that of pure Fe.

2.1.4 Other Iron Alloys

Other Fe-Ni systems that have been studied include alloys of Fe, Ni, and at least one light element. For example, high-pressure studies focusing on compressional wave velocity showed hexagonal close-packed (hcp) Fe-Ni-Si to be a possible composition of Earth's inner core (Liu *et al.*, 2015). In terms of electrical resistivity, Stacey and Anderson (2001)

found the effect of Si to be the same as Ni on a weight percentage basis in Fe-Ni-Si ternary alloys. Zhang *et al.* (2021) measured the electrical resistivity of Fe-10wt%Ni at ~80-140 GPa and up to 3400 K in the diamond anvil cell with applications to Earth's outer core (see Figure 2.1). The effect of Ni on the resistivity of the alloy compared with pure Fe at these high pressures and temperatures was relatively minor as shown in Fig. 1 and at conditions representative of Earth's CMB, ~142 GPa and 3000 K, they appear to be the same.
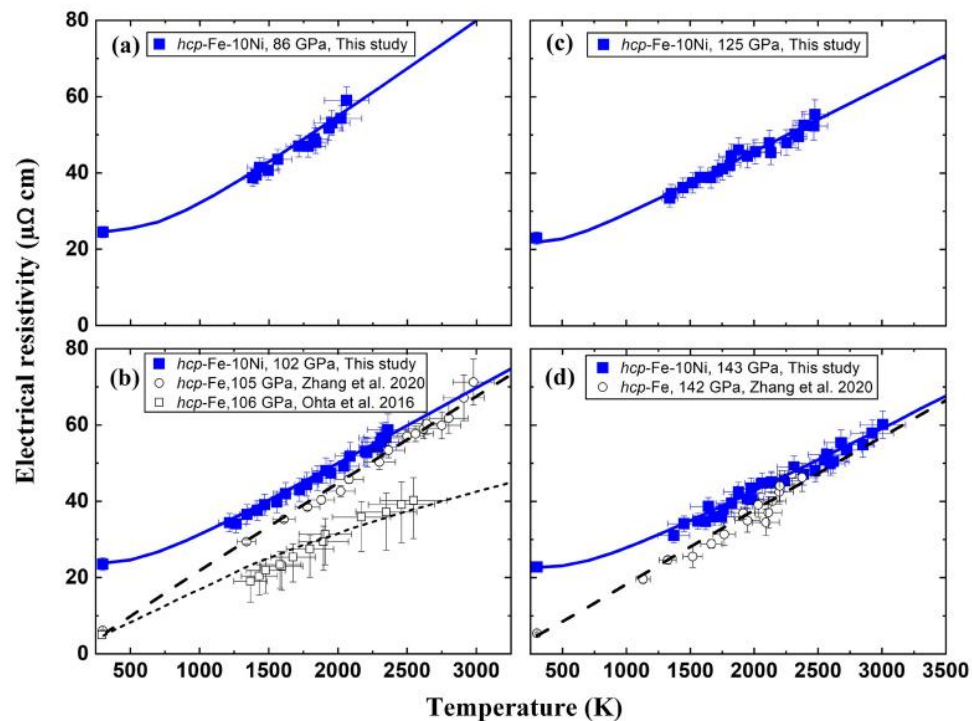
Figure 2.1: Resistivity of Fe-10wt%Ni found by Zhang *et al.*, 2021 at four pressures 86-143 GPa shown in filled blue circles (a-d) and compared to pure Fe shown in open black circles (b,d)

Additionally, electrical resistivity research has been performed on alloys of Fe with light elements, especially Si. Iron alloys with 4.5% Si, for example, studied at pressures as high as 24 GPa using a multi-anvil press have shown similar electrical resistivity results as pure Fe (Silber *et al.*, 2019). High pressures can also induce resistivity saturation as has been observed in 17% Si (Kiarasi and Secco, 2015). Experiments up to 100 GPa at ambient temperature on Fe and Fe-4at%Si show a large effect of Si impurity, with the

resistivity at each pressure more than doubling (Gomi *et al.*, 2013). The alloying effect of 15at% Si approximately doubles the electrical resistivity (or halves the thermal conductivity) of Fe at conditions near the top of Earth's core (Hsieh *et al.*, 2020).

Other light elements that have been studied at high pressures in alloys with Fe include S, O, and Mg. The effect of S on electrical resistivity of liquid Fe has been shown to be stronger than that of Si (Pommier, 2018). Similarly, Fe-S liquid is more resistive than Fe-Si-S liquid (Pommier *et al.*, 2019), though more recent work suggests not as much as previously thought (Littleton *et al.*, 2021). Electrical resistivity studies of various alloys of Fe-5wt%S with 3wt% each or less of O, Mg, and Si found a wide range of resistivities (~200-1500 $\mu\Omega \cdot$cm) (Pommier *et al.*, 2020).

2.2 Theoretical Approaches

To improve our estimates of electrical resistivity of liquid alloys, theoretical models of molecular structure and electron transport are another important method. It is worth mentioning a few types of methods in particular: molecular dynamics, *ab initio* studies, and density functional theory. Molecular dynamics (MD) studies were some of the first computational models to be developed for this area. Models are constructed of individual molecules interacting with their neighbors for a short amount of time on the order of nanoseconds, giving a result about the dynamics of the particles (e.g., Belashchenko, 2013). In general, *ab initio* studies are those that derive the inter-particle interactions based on first principles, such as quantum mechanics, rather than on empirical observations, such as inter-atomic potentials and are preferable from a theorist's standpoint.

Density functional theory (DFT), on the other hand, focuses on the density of electrons throughout a conductive metal (Kohn and Sham, 1965). Understanding electron density is particularly useful for resistivity measurements because electron scattering increases the resistivity of a material. In Fe-10wt%Ni, the case of interest for this research, where the electron configurations of the end members are Fe ([Ar] $3d^6$ $4s^2$) and Ni ([Ar] $3d^8$ $4s^2$), each has unfilled 3d bands. The s$\rightarrow$d scattering, where s-conduction electrons get scattered into empty d-bands, is dominant for these metals (Mott, 1972).

To determine the stable phase of a metal (e.g., hcp Fe), one technique used within DFT is minimizing the Helmholtz free energy. The free energy is calculated from contributions by both static components, such as electron excitations and the lattice, and vibrational components, such as phonons (e.g., Ekholm *et al*., 2011). Such techniques have found the electrical resistivity and thermal conductivity of body-centered cubic (bcc) and hcp Fe (Sha and Cohen, 2011) and found that the effect of alloying 5-15at% Ni on the structure of Fe has differing effects depending on temperature (Ekholm *et al.,* 2011). In the range of 4000-8000 K, Ni is predicted to act as a stabilizing agent for the hcp phase. In contrast, at lower temperatures, Ni acts as a stabilizing agent for the face-centered cubic (fcc) phase, in agreement with experimental results.

Light element candidates in the core have electronic structures differing from Fe and Ni, resulting in significant consequences for electrical resistivity of alloys. The addition of O or Si to Fe is predicted by the (DFT-based) Kubo-Greenwood formula to increase the expected electrical resistivity of Fe (Pozzo *et al.*, 2012) because of the added impurity scattering. Additionally, the conductivities of various alloys of Fe-10wt%Ni with light elements including H, C, O, Si, and S have been studied theoretically using a DFT-based method. These elements tend to increase the alloy's resistivity until their proportion of the alloy reaches 30wt%, at which point resistivity saturation is reached (Zidane *et al.*, 2020). Similar models based on MD have shown similar effects of light elements on liquid iron alloys (Wagle *et al.*, 2018; Ohmura *et al.*, 2020).

2.3 Concluding Remarks

Clearly, electrical resistivity studies of Fe alloys can have important implications for heat flow through planetary body cores. For example, the addition of 3wt%O to FeS leads to an addition of at least 1 Gy to the modeled duration of the Martian dynamo (Pommier *et al.*, 2020). A combination of experimental results and density functional theory and other theories (e.g., Gomi and Hirose, 2015) is crucial for extrapolating and interpolating results beyond what is experimentally feasible.

While both experimental and theoretical studies have been performed on the resistivity of Fe-10wt%Ni, a few aspects of this study have unique merit. For one, while Zhang *et al*.

(2020) did measure the resistivity of Fe-10wt%Ni into the liquid state at high pressures, the lowest pressure of experimentation was 80 GPa. While such pressures are closer to those at Earth's CMB than those in this study, the lower pressures of this study (2-5 GPa) are closer to the CMB of small terrestrial bodies. Additionally, many of the very high-pressure experiments on Fe-10wt%Ni were performed in a diamond-anvil cell. The cubic anvil press of this study has complementary strengths to a diamond-anvil cell (e.g., Liebermann, 2011), such as avoiding large temperature and pressure gradients, and thus can provide important low pressure data to which higher pressure data must be anchored.

References

Anzellini, S., Dewaele, A., Mezouar, M., Loubeyre, P., Morard, G. 2013. Melting of Iron at Earth's Inner Core Boundary Based on Fast X-ray Diffraction. *Science*. 340: 464-466.

Belashchenko, D.K. 2013. Computer Simulations of Liquid Metals. *Physics Uspekhi*. 56: 1176.

Deng, L., Seagle, C., Fei, Y., Shahar, A. 2013. High pressure and temperature electrical resistivity of iron and implications for planetary cores. *Geophysical Research Letters*. 40: 33-37.

Ekholm, M., Mikhaylushkin, A.S., Simak, S.I., Johansson, B., Abrikosov, I.A. 2011. Configurational thermodynamics of Fe–Ni alloys at Earth's core conditions. *Earth and Planetary Science Letters*. 308: 90-96.

Gomi, H., Ohta, K., Hirose, K., Labrosse, S., Caracas, R., Verstraete, M.J., Hernlund, J.W. 2013. The high conductivity of iron and thermal evolution of the Earth's core. *Physics of the Earth and Planetary Interiors*. 224: 88-103.

Gomi, H., and Hirose, K. 2015. Electrical resistivity and thermal conductivity of hcp Fe–Ni alloys under high pressure: Implications for thermal convection in the Earth's core. *Physics of the Earth and Planetary Interiors*. 247: 2-10.

Ioffe, A.F., and Regel, A.R. 1960. *Progress in Semiconductors*. 4: 237.

Ito, E. 2015. Multi-Anvil Cells and High-Pressure Experimental Methods. *Treatise on Geophysics*. 233-258.

Hsieh, W.-P., Goncharov, A.F., Labrosse, S., Holtgrewe, N., Lobanov, S.S., Chuvashova, I., Deschamps, F., Lin, J.-F. 2020. Low thermal conductivity of iron-silicon alloys at Earth's core conditions with implications for the geodynamo. *Nature Communications*. 11: 3332.

Huang, E., Bassett, W.A., Weathers, M.S. 1988. Phase relationships in Fe-Ni alloys at high pressures and temperatures. *Journal of Geophysical Research*. 93: 7741-7746.

Kiarasi, S., and Secco, R.A. 2015. Pressure-induced electrical resistivity saturation of Fe17Si. *Physica Status Solidi B*. 252: 2034–2042.

Kita, Y., and Morita, Z. 1984. The Electrical Resistivity of Liquid Fe-Ni, Fe-Co and Ni-Co Alloys. *Journal of Non-Crystalline Solids*. 61: 1079-1084.

Kuznetsov, A.Yu., Dmitriev, V., Volkova, Y., Kurnosov, A., Dubrovinskaia, N., Dubrovinsky, L. 2007. In-situ combined X-ray diffraction and electrical resistance measurements at high pressures and temperatures in diamond anvil cells. *High Pressure Research*. 27: 213-222.

Liebermann, R.C. 2011. Multi-anvil, high pressure apparatus: a half-century of development and progress. *High Pressure Research*. 31: 493-532.

Lin, J.-F., Heinz, D.L., Campbell, A.J., Devine, J.M., Mao, W.L., Shen, G. 2002. Iron-Nickel alloy in the Earth's core. *Geophysical Research Letters*. 29: 1471.

Littleton, J.A.H., Secco, R.A., Yong, W. 2021. Electrical Resistivity of FeS at High Pressures and Temperatures: Implications of Thermal Transport in the Core of Ganymede. *Journal of Geophysical Research*. 126: p. n/a.

Liu, J., Lin, J., Alatas, A., Hu, M.Y., Zhao, J., Dubrovinsky, L. 2015. Seismic parameters of hcp-Fe alloyed with Ni and Si in the Earth's inner core. *Journal of Geophysical Research: Solid Earth*. 121: 610-623.

Mott, N.F. 1972. The electrical resistivity of liquid transition metals. *The Philosophical Magazine: A Journal of Theoretical Experimental and Applied Physics.* 26: 1249-1261.

Ohmura, S., Tsuchiya, T., Shimojo, F. 2020. Structures of Liquid Iron–Light-Element Mixtures under High Pressure. *Physical Status Solidi B.* 257: 2000098.

Ohta, K., Kuwayama, Y., Hirose, K., Shimizu, K., Ohishi, Y. 2016. Experimental determination of the electrical resistivity of iron at Earth's core conditions. *Nature*. 534: 95-97.

Pommier, A. 2018. Influence of sulfur on the electrical resistivity of a crystallizing core in small terrestrial bodies. *Earth and Planetary Science Letters*. 496: 37-46.

Pommier, A., Leinenweber, K., Tran, T. 2019. Mercury's thermal evolution controlled by an insulating liquid outermost core? *Earth and Planetary Science Letters*. 517: 125-134.

Pommier, A. 2020. Experimental Investigation of the Effect of Nickel on the Electrical Resistivity of Fe-Ni and Fe-Ni-S Alloys under Pressure. *The American Mineralogist*. 105: 1069-1077.

Pommier, A., Davies, C.J., Zhang, R. 2020. A Joint Experimental-Modeling Investigation of the Effect of Light Elements on Dynamos in Small Planets and Moons. *Journal of Geophysical Research: Planets.* 125: p. n/a.

Pozzo, M., Davies, C., Gubbins, D., Alfè, D. 2012. Thermal and electrical conductivity of iron at Earth's core conditions. *Nature.* 485: 355–358.

Secco, R.A., and Schloessin, H.H. 1989. The electrical resistivity of solid and liquid Fe at pressures up to 7 GPa. *Journal of Geophysical Research: Solid Earth*. 94: 5887-5894.

Sha, X., and Cohen, R.E. 2011. First-principles studies of electrical resistivity of iron under pressure. *Journal of Physics: Condensed Matter*. 23: 075401.

Silber, R.E., Secco, R.A., Yong, W. 2017. Constant electrical resistivity of Ni along the melting boundary up to 9 GPa. *Journal of Geophysical Research: Solid Earth*. 122: 5064-5081.

Silber, R.E., Secco, R.A., Yong, W., Littleton, J.A.H. 2018. Electrical resistivity of liquid Fe to 12 GPa: Implications for heat flow in cores of terrestrial bodies. *Scientific Reports*. 8: 10758-9.

Silber, R.E., Secco, R.A., Yong, W., Littleton, J.A.H. 2019. Heat Flow in Earth's Core From Invariant Electrical Resistivity of Fe-Si on the Melting Boundary to 9 Gpa: Do Light Elements Matter? *Journal of Geophysical Research: Solid Earth*. 124: 5521-5543.

Stacey, F.D., and Anderson, O.L. 2001. Electrical and thermal conductivities of Fe–Ni–Si alloy under core conditions. *Physics of the Earth and Planetary Interiors*. 124: 153-162.

Wagle, F., Steinle-Neumann, G., de Koker, N. 2018. Saturation and negative temperature coefficient of electrical resistivity in liquid iron-sulfur alloys at high densities from first-principles calculations. *Physical Review B*. 97: 094307.

Yong, W., Secco, R.A., Littleton, J.A.H., Silber, R.E. 2019. The Iron Invariance: Implications for Thermal Convection in Earth's Core. *Geophysical Research Letters*. 46: 11065-11070.

Zhang, Y., Hou, M., Liu, G., Zhang, C., Prakapenka, V.B., Greenberg, E., Fei, Y., Cohen, R.E., Lin, J.-F., 2020. Reconciliation of experiments and theory on transport properties of iron and the geodynamo. *Physical Review Letters*. 125: 078501.

Zhang, Y., Hou, M., Driscoll, P., Salke, N.P., Liu, J., Greenberg, E., Prakapenka, V.B., Lin, J.-F., 2021. Transport properties of Fe-Ni-Si alloys at Earth's core conditions: Insight into the viability of thermal and compositional convection. *Earth and Planetary Science Letters*. 553: 116614.

Zidane, M, Salmani, E.M., Majumdar, A., Ez-Zahraouy, H, Benyoussef, A., Ahuja, R. 2020. Electrical and thermal transport properties of Fe–Ni based ternary alloys in the earth's inner core: An ab initio study. *Physics of the Earth and Planetary Interiors*. 301: 106465.

Chapter 3

3 Implications for the Energy Source for an Early Dynamo in Vesta from Experiments on Electrical Resistivity of Liquid Fe10Ni at High Pressures

A version of this chapter is being submitted for publication.

3.1 Introduction

The processes driving the magnetic fields of various planetary bodies are still not fully understood (e.g., Bushby *et al.*, 2018; Pommier *et al.*, 2020). For the terrestrial planets, the likeliest mechanism responsible for each of the past and present magnetic fields is, in most cases, a form of convection in the core fluid. For Earth, the convective movement of electrical charge in the liquid outer core is likely in helical Taylor columns roughly parallel with the Earth's axis of rotation (Roberts, 1968; Busse, 1970) that causes a dynamo effect and which generates a magnetic field (Larmor, 1919). Similar mechanisms may generate a magnetic field in terrestrial planetary bodies throughout their histories under certain core conditions. Because the motion in liquid planetary cores may be driven in part by thermal convection at some stage of their evolution, most models of planetary magnetic field generation require estimates of heat transfer mechanisms through planetary cores.

When considering the total heat flow at the top of the liquid region of the core of a planetary terrestrial body, the portion due to thermal convection may be derived by comparison of estimates of heat flow across its core-mantle boundary (CMB) and the adiabatic heat flow at the top of its core. The total adiabatic heat flow can easily be derived if thermal conductivity of the core material and the core temperature gradient are known. Our experiments constrain a value of thermal conductivity.

Thermal conductivity of metals can be calculated as a function of the more easily measured electrical resistivity through the Wiedemann-Franz Law (Wiedemann and Franz, 1853):

$$\rho = LT/\kappa \quad \text{(Eq. 3.1)}$$

where the electrical resistivity (ρ) at a specific temperature (T) is related to its thermal conductivity (κ) via the Lorenz number ($L = 2.44 \times 10^{-8}$ WΩK^{-2}). The Lorenz number for Fe-Ni alloys may increase with temperature (Klemens and Williams, 1986). If estimates of pressure and composition at the top of the core of a given differentiated planetary body are known or estimated, then the electrical resistivity of such a composition may be experimentally measured in its liquid state at the given pressure. From this measured property, thermal conductivity may be calculated.

At the pressures of the experiments reported here, a relevant terrestrial-type body is asteroid 4-Vesta. The *Dawn* mission to the Asteroid Belt discovered that Vesta possesses a differentiated core of estimated radius 110±3 km or depth of ~153 km (Russell *et al.*, 2012, Ermakov *et al.*, 2014) and composition of ~92% Fe and ~8% Ni by weight (Dreibus *et al.*, 1997). Vesta, the second-largest object in the main Asteroid Belt, is thought to have formed early in the life of the solar system, as early as 2 million years after the formation of the calcium-aluminum-rich inclusions (McSween and Huss, 2010). As such, Vesta is one of few preserved protoplanets from the early solar system to have survived through all mass depletions of the Asteroid Belt such as the Late Heavy Bombardment (e.g., O'Brien and Sykes, 2011).

Vesta is thought to have once possessed an internally generated magnetic field, as evidenced by paleomagnetism in meteorites from Vesta (Fu *et al.*, 2012). The Howardite-Eucrite-Diogenite (HED) class of meteorites are widely (though not universally (Wasson, 2013)) accepted to have originated from Vesta due to close similarities in spectral reflectivity (McCord *et al.*, 1970; Consolmagno and Drake, 1977), the abundance of Vesta family asteroids (Binzel and Xu, 1993), and comparative mineralogy (Russell *et al.*, 2012). Natural remanent magnetism and ^{40}Ar/^{39}Ar plateau radiometric dating of a eucrite meteorite show that Vesta's surface experienced a magnetic field intensity of 2 μT as late as 3.69 billion years ago (Fu *et al.*, 2012). This magnetism may have been either generated directly by Vesta's core dynamo or caused by crustal magnetism due to a past core dynamo on Vesta. Less likely possibilities include Vesta passing closely by the magnetic field of Jupiter, a distance of 2.4 AU currently. Vesta's core dynamo is estimated to have had a peak surface intensity between 10 and 100 μT (Fu *et al.*, 2012)

and its present day crustal magnetism of $> 0.2\ \mu T$ is likely to have been preserved due to a lack of space weathering (Vernazza *et al.*, 2006).

One or more mechanisms may have been responsible for the stirring of the core liquid that generated the early Vestan internal dynamo. First, thermal convection may have churned the liquid core as heat was convectively transferred in the liquid core to the CMB where it was conducted to the mantle. Second, if a nearly pure Fe solid inner core formed within a liquid outer core, compositional convection could have driven a dynamo in Vesta (Formisano *et al.*, 2016) as it does in the Earth today (e.g., Glatzmaier and Roberts, 1996; Driscoll and Du, 2019). An additional complicating factor, but also another stirring mechanism, is the possibility of the cores of small bodies such as Vesta freezing from the top inward rather than from the center outward as Earth's core does (e.g., Williams, 2009). Compositional convection is estimated to be capable of producing a dynamo in cores with minimum radii of ~90 km (Nimmo, 2009), which is similar to the radius of Vesta's core. In this study, we focus on determining if thermal convection was a possible stirring mechanism in the early Vestan core by measuring high-pressure electrical resistivity of liquid Fe-Ni alloys.

3.2   Methods

The electrical resistivity of Fe10Ni was measured at integer pressures in the range 2-5 GPa and at temperatures into the liquid state. Samples were obtained from ChemPur Feinchemikalien und Forschungsbedarf GmbH. The average and standard deviation of nine electron microprobe analyses of the starting material showed it to be 90.29 ± 0.14 wt%Fe and 9.65 ± 0.70 wt%Ni. All experiments were conducted in a 1000-ton cubic anvil press (Secco, 1995) with manually controlled heating capabilities. The pressure cell, as shown in Figure 3.1, used the four-wire resistivity technique which is essential for accurate resistivity measurements of a metal. One pair of opposite sides of the cube conducted a high alternating current of ~250 A through a graphite furnace to heat the sample. The other two pairs of opposing sides, contacting the anvil faces with a copper disk, each completed a circuit with a W5%Re-W26%Re thermocouple inside the pressure cell. In addition to measuring temperature, these thermocouple wires also served as electrodes to make the resistance measurement. By passing a constant current of 0.2 A

from a Keysight B2961A power source through the electrodes and sample, the voltage drop, and thereby the resistance of the sample, was measured. More details and diagrams may be found about the wiring design in Figure 3.1 and about the sample wire configuration and emplacement in Littleton *et al*. (2018). A few modifications as follows applied to these experiments.
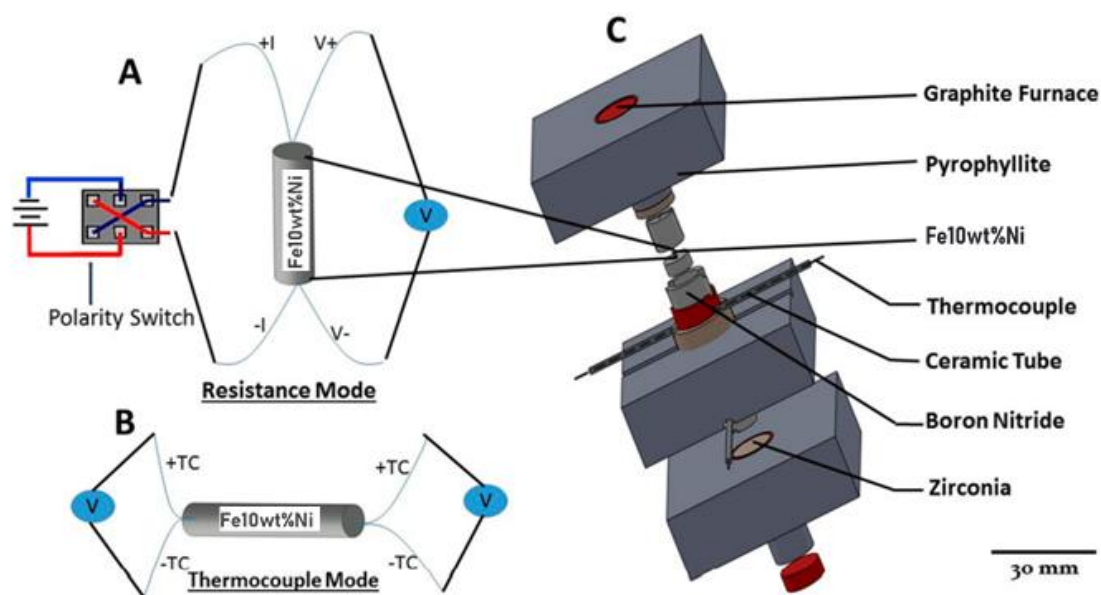
Figure 3.1: Drawing of the pressure cell design (modified from Ezenwa and Secco (2017)); (A) The 4-wire method of measuring resistance; (B) Wiring of the thermocouples; (C) Components of a three-sectioned pressure cell

In each experiment, once the pressure stabilized at the desired value, temperature in the cell was increased to ~800-1000 K below the melting T, to ensure contact between various metal parts. Temperature was then decreased to room T and then increased incrementally for resistivity measurement. At each measurement T, with intervals of 50 K in the solid state and less than 20 K in the liquid state, a Keysight 34470A data acquisition meter operating at 20 Hz recorded the voltage drop across the sample with 1 μV resolution. Multiple voltage readings (generally between ten and twenty) for both positive and negative currents were obtained using a current polarity switch which was employed to remove any parasitic potentials. These voltage readings were averaged into a single data point per temperature value, each of which was used to determine the

resistivity of Fe10Ni as a function of temperature and pressure. The standard deviation of the voltage measurements was included in error estimates. Additional experimental details and images may be found in Appendix A.

After each high-pressure experiment, the sample was recovered and analyzed. The BN sleeve was manually polished parallel to its longitudinal axis to expose the sample. Photographs were taken under a Nikon SMZ2800 microscope at various stages of polishing and repeated measurements of diameter and length of the sample were made on the cross-section as polishing approached the center. Finally, the chemical composition of the sample was measured in multiple locations using a JEOL JXA-8530F field-emission electron microprobe with a 60 nA probe current, 15 kV accelerating voltage, and 10 µm spot-size beam.

To calculate resistivity of the sample material as a function of the measured voltage, Ohm's and Pouillet's Laws were employed. Ohm's Law describes the resistance (R), an extensive property of the sample, as a function of the voltage drop (V) and current (I) through the sample: $R = V/I$. Pouillet's Law, $\rho = R * A/L$, then determines the electrical resistivity, an intensive property of the material, for the sample's cross-sectional area A and length L. Additionally, the electrical resistance of the Pt disks above and below the sample were considered as part of the series circuit for Ohm's Law, though the disks had minimal contribution. The resistivity of Pt at experimental temperatures and pressures were extrapolated from values calculated by density functional theory (Gomi and Yoshino, 2019) in order to remove its minor contribution to the measured resistance values.

Various sources of error were considered for estimating the error of each resistivity measurement. For example, in the geometrical measurements of the circuit components, the Pt disks, and the Fe10Ni sample, an error of ~10 µm was typical. The standard deviations from averaging the voltage and temperature data were assessed for each resistivity data point. Small fluctuations in the current from the power source also may have contributed error, though these are expected to be negligible amounts in

comparison. For thermal conductivity calculations, uncertainty in the Lorenz number further contributed to error values. Error was propagated using standard methods.

3.3   Results and Discussion

3.3.1   Fe10Ni Experiments

Post-experimental analysis of the samples involved geometrical measurements under a visible light microscope and Electron Microprobe Analysis (EMPA). **Error! Reference source not found.** displays images of the same recovered sample at roughly the same scale but using visible light (2a) and back-scattered electron (BSE) (2b) imaging, with corresponding compositions in Table 3.1. Both **Error! Reference source not found.** and Figure 3.3 show the BSE images of an Fe10Ni sample after exposure to 5 GPa. The difference is recovery temperature, with the sample in **Error! Reference source not found.** recovered just above melting and the sample in Figure 3.3 recovered just below melting. **Error! Reference source not found.**a shows that even at temperatures in the liquid state, the sample is well-contained and maintains its cylindrical geometry. As Table 3.2 shows, the Fe composition is 90±1% at almost all points probed, even near the boundary with the Pt disks. Therefore, EMPA results show little to no contamination of the sample and the Pt disks when the temperature is near the melting temperature of Fe10Ni. At temperatures significantly above the melting temperature, where both temperature and time spent in the liquid state are important, Pt from the disks begins to diffuse into the sample as shown by the probe results in **Error! Reference source not found.**c. However, as later discussed in application to Vesta, the results used to calculate heat flow are those just after melting which ensure a composition very close to the starting sample composition.
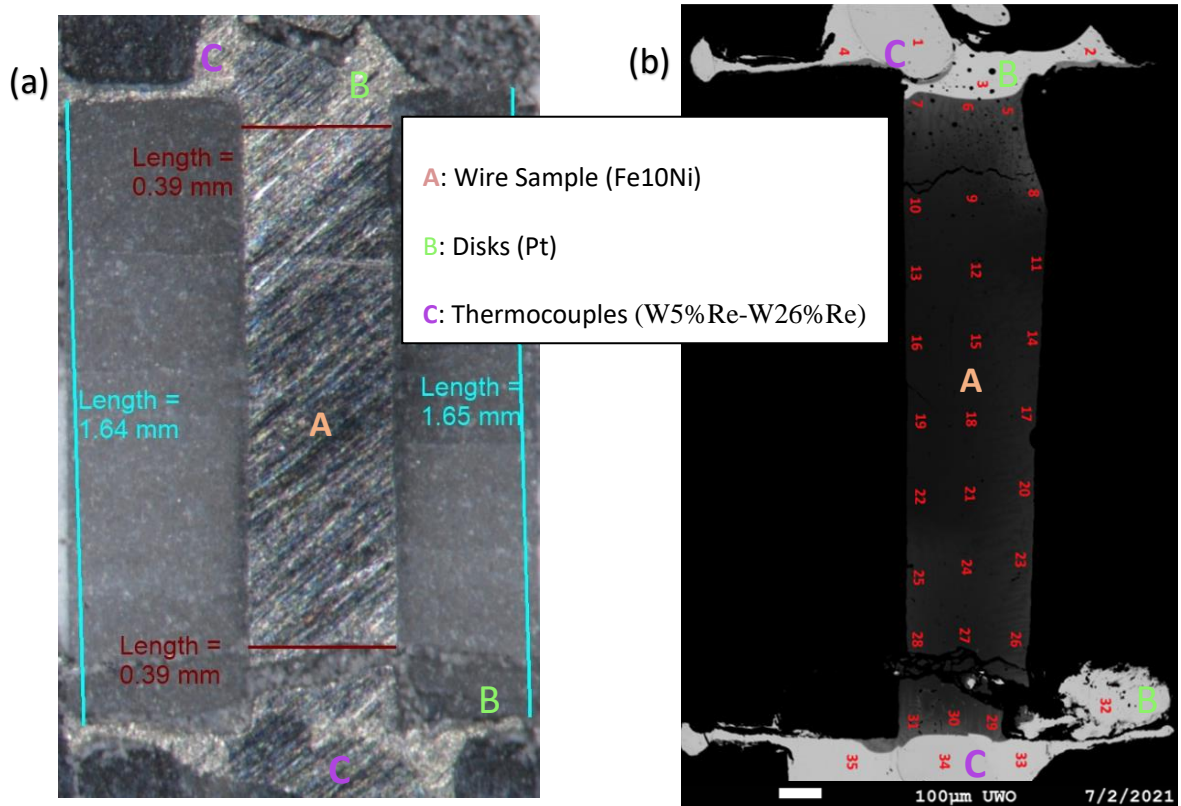
Figure 3.2: (a) Visible light cross-sectional image of Fe10Ni recovered from 5 GPa and 1853 K (~60 K above melting T) (b) Back-scattered electron image of the same sample after polishing

Table 3.1: Electron microprobe results corresponding to points on the image in Figure 3.2b

Point	Fe(Mass%)	Re(Mass%)	Pt(Mass%)	Ni(Mass%)	W(Mass%)	Total(Mass%)
1	0.002	25.005	0.277	nd	74.027	99.311
2	nd	nd	99.815	0.002	nd	99.817
3	0.008	nd	99.915	nd	nd	99.923
4	0.013	nd	99.55	nd	nd	99.563
5	60.856	0.112	31.113	6.63	0.649	99.36

6	59.162	0.581	32.814	6.189	1.732	100.478
7	61.887	0.647	27.476	7.002	2.965	99.977
8	70.839	0.292	19.694	7.672	0.802	99.299
9	82.612	0.115	7.468	8.538	0.452	99.185
10	83.641	0.204	6.7	8.413	0.648	99.606
11	85.67	nd	4.646	8.772	0.137	99.225
12	84.854	0.12	4.175	9.862	0.297	99.308
13	87.369	nd	2.904	8.748	0.186	99.207
14	80.541	0.229	10.306	8.371	0.604	100.051
15	85.007	nd	3.997	9.698	0.536	99.238
16	86.89	nd	2.466	9.835	0.206	99.397
17	78.388	0.094	11.686	8.483	0.8	99.451
18	85.715	0.12	3.102	9.303	0.692	98.932
19	86.733	0.022	1.976	9.812	0.101	98.644
20	74.587	0.131	15.459	8.237	0.68	99.094
21	85.398	0.258	2.558	9.822	1.037	99.073
22	85.144	nd	1.807	10.6	0.51	98.061
23	74.716	0.162	15.348	8.515	0.83	99.571
24	80.534	1.003	7.167	8.195	2.728	99.627
25	76.615	2.211	7.798	7.782	5.057	99.463
26	73.77	0.579	17.225	7.584	1.357	100.515
27	81.823	0.393	7.488	8.692	1.275	99.671
28	76.582	1.709	8.52	8.166	4.498	99.475
29	65.51	1.131	20.259	7.467	5.381	99.748

30	64.57	5.035	12.856	6.604	10.595	99.66
31	57.144	6.638	12.37	5.977	17.218	99.347
32	0.004	nd	100.151	nd	nd	100.155
33	0.016	nd	99.983	0.008	nd	100.007
34	nd	24.962	0.198	0.005	74.293	99.458
35	0.005	nd	100.35	0.001	nd	100.356
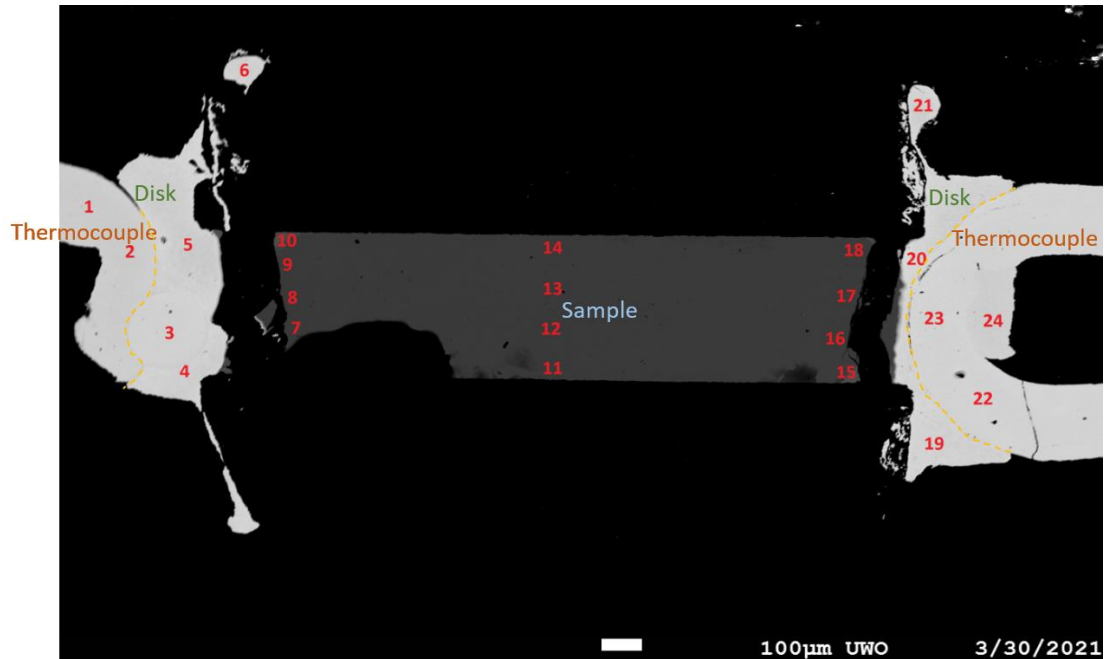
Figure 3.3: Back-scattered electron image showing Fe10Ni sample (dark grey) in the center with Pt disks and W5%Re-W26%Re thermocouple (light grey) on each end separated by dashed lines. This sample was used only for compositional analyses to demonstrate the lack of contamination before melting. This sample was not used for resistivity determination.

Table 3.2: Chemical composition of sample in Figure 3.3 from 5 GPa and 1781 K (~10 K below the melting T)

Point	Fe(Mass%)	Re(Mass%)	Pt(Mass%)	Ni(Mass%)	W(Mass%)	Total(Mass%)
1	nd	3.565	0.351	0.001	93.348	97.265
2	0.002	4.082	0.318	0.015	90.505	94.922
3	nd	24.606	0.275	0.005	71.163	96.049
4	nd	nd	97.551	0.003	0.03	97.584
5	nd	nd	97.455	0.01	nd	97.465
6	nd	nd	97.41	nd	nd	97.41
7	89.249	nd	0.019	9.384	nd	98.652
8	89.206	nd	nd	9.077	nd	98.283
9	88.715	0.048	0.002	9.394	0.016	98.175
10	80.188	nd	7.663	10.1	0.651	98.602
11	89.035	nd	nd	9.482	nd	98.517
12	89.15	nd	nd	9.558	nd	98.708
13	88.644	nd	nd	9.474	nd	98.118
14	90.249	nd	nd	9.48	nd	99.729
15	89.508	nd	nd	9.465	0.011	98.984
16	89.774	nd	0.014	9.375	nd	99.163
17	89.1	nd	nd	9.56	nd	98.66
18	90.133	nd	0.007	9.401	nd	99.541
19	0.015	nd	96.148	0.007	nd	96.17
20	0.018	0.017	96.471	nd	nd	96.506
21	nd	nd	94.626	nd	nd	94.626
22	nd	24.58	0.207	nd	72.971	97.758
23	0.017	24.485	0.292	0.004	71.196	95.994

| 24 | nd | 4.48 | 0.299 | 0.001 | 89.969 | 94.749 |

In Figure 3.4, the electrical resistivity of Fe10Ni as a function of temperature up to ~300 K above the melting temperatures is displayed. Figure 3.4a shows the data from one experimental run at 3 GPa to avoid clutter, while Figure 3.4b shows data from 2-5 GPa along with comparable data of pure Fe (Silber *et al.*, 2018) and pure Ni (Silber *et al.*, 2017) respectively. The first inflection at ~800 K corresponds to both a magnetic transition and the change from a bcc (α) structure to an fcc (γ) structure. The second inflection at ~1750 K corresponds to melting. As anticipated, electrical resistivity increases near-monotonically with temperature and decreases in general with pressure. The zoom-in of the region just after melting shown in Figure 3.4c is the temperature range that is most relevant to planetary fluid cores. For all the Fe10Ni resistivity data used in Figure 3.4, as well as EMPA results for the Fe10Ni samples used, see Appendix B.2.

(a)

(b)
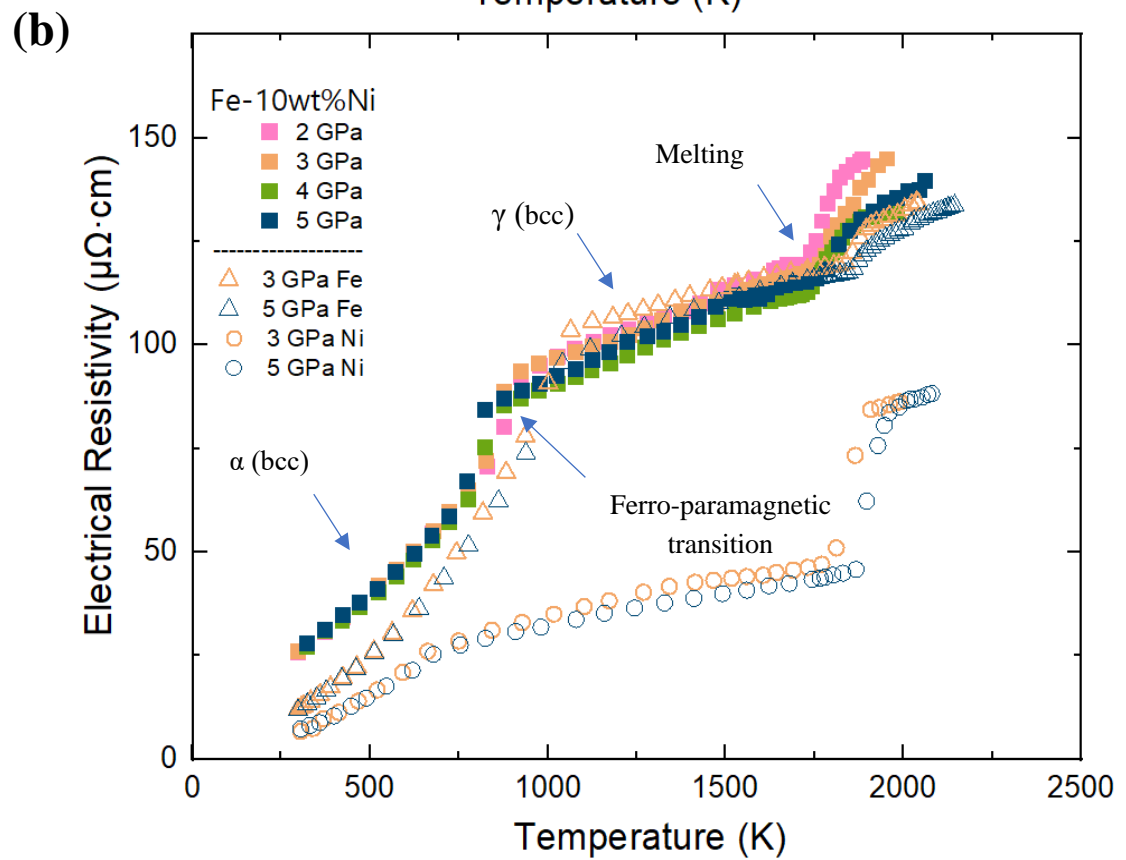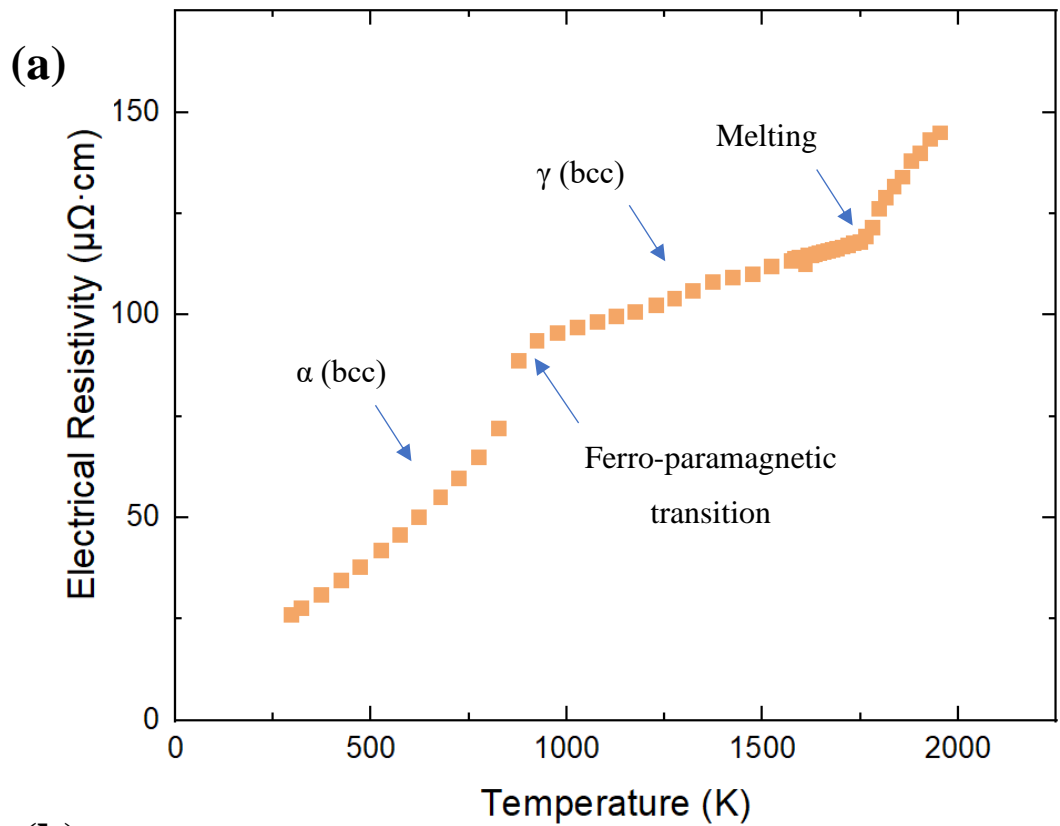
(c)
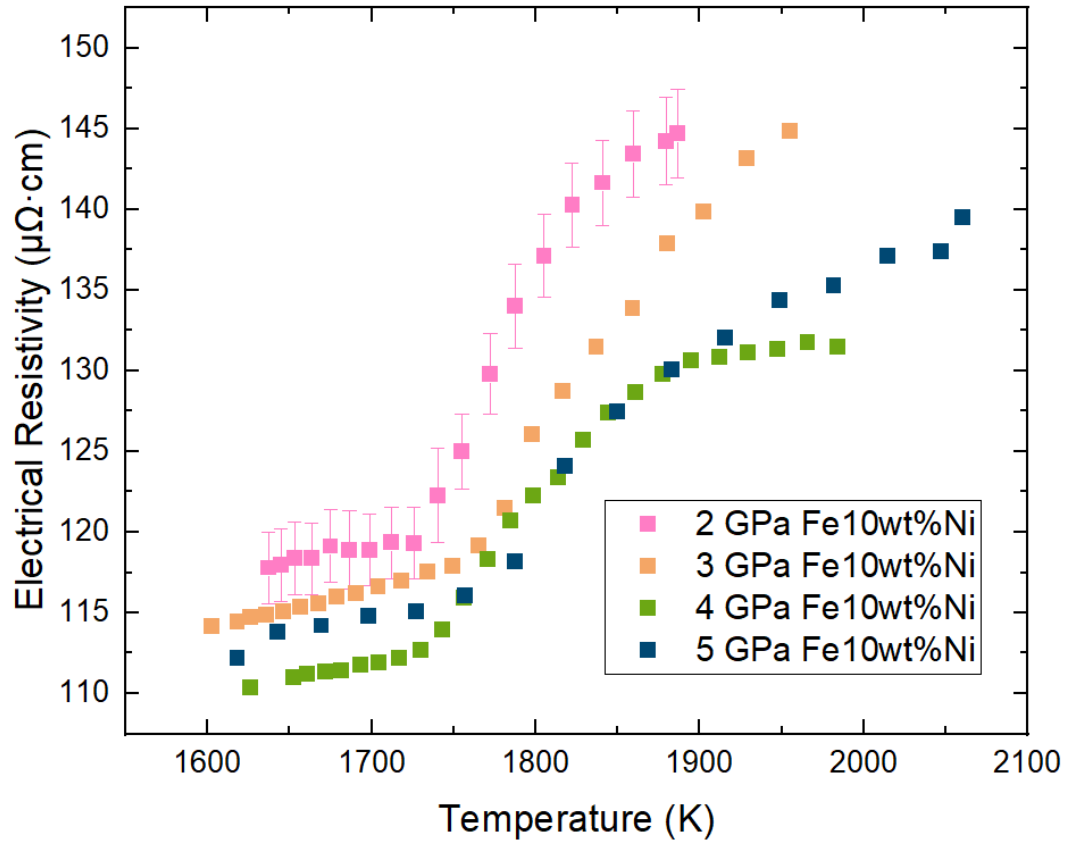
Figure 3.4: Electrical resistivity of Fe10Ni as a function of temperature at pressures 2-5 GPa. (a) Data at 3 GPa alone is shown as an example. (b) Data for Fe (Silber *et al.*, 2018) and for Ni (Silber *et al.*, 2017) are shown for comparison. (c) A zoom-in of temperatures near melting is shown with representative measurement error bars shown for the 2 GPa data.

With our resistivity data, the Wiedemann-Franz Law was used to calculate thermal conductivity as a function of temperature (see Eq. 1). The electronic component of thermal conductivity for metals dominates over the lattice or phonon thermal conductivity (Klemens and Williams, 1986). The Lorenz number may vary with pressure, but the Sommerfeld value used is a reasonable approximation at the temperatures and pressures of this study. As shown in Figure 3.5, thermal conductivity increases

monotonically between the α-γ phase change of Fe10Ni (~800 K) and the melting (~1700 K) but decreases suddenly at the start of melting.

In Figures 3.4 and 3.5, the data for 5 GPa do not quite follow the trend of resistivity decreasing with pressure formed by the other 3 pressure runs. The overlap between the resistivity (and thermal conductivity) curves at 5 GPa and 4 GPa is most likely due to experimental error, since the estimated error is larger than this anomaly. The source of this error could be, for example, statistical error in collecting data or measurement error in machining parts for the pressure cell. Additionally, the proportional difference between 5 GPa and 4 GPa is smaller than that between 3 GPa and 2 GPa, which could contribute to this effect.
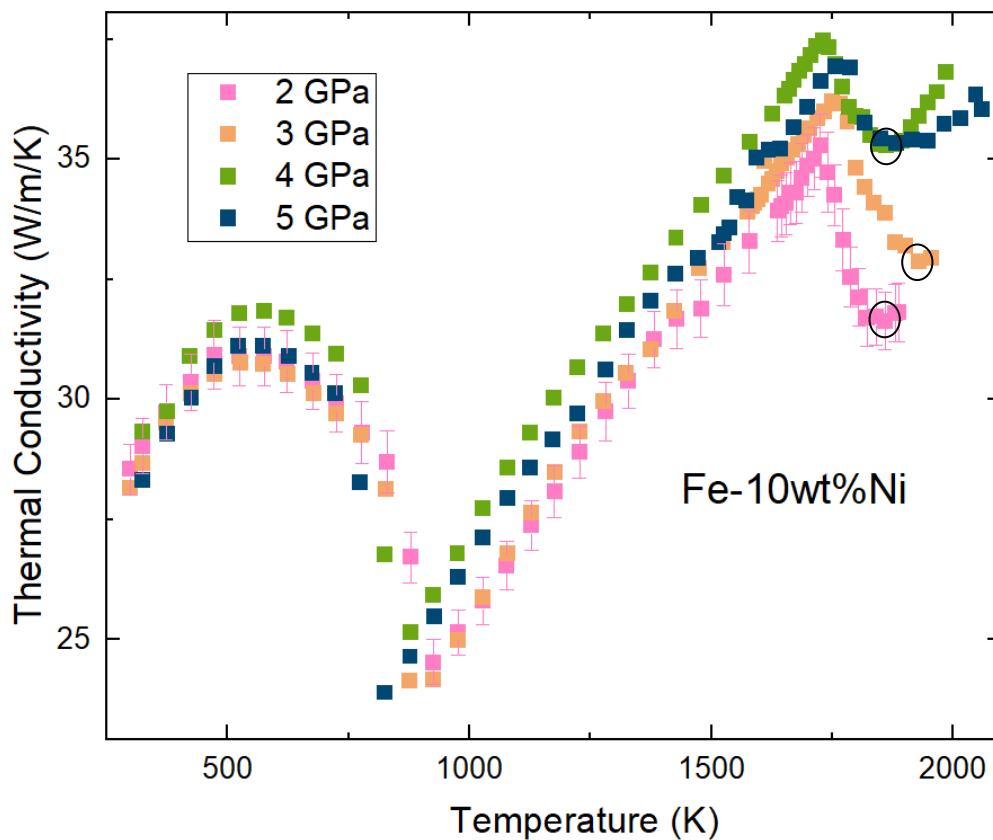
Figure 3.5: Thermal conductivity plotted with respect to temperature at pressures in the range 2-5 GPa. Points used for applications to early Vesta are circled.

3.3.2   Applications to Vesta

With thermal conductivity of Fe10Ni known, the adiabatic or conducted heat flux at the top of the core of a terrestrial body of this composition may be estimated using thermodynamics. By Fourier's Law for heat transfer:

$$q = -\kappa \nabla T \quad \text{(Eq. 3.2)}$$

where local heat flux density is q and the radial temperature gradient, ∇T, may be estimated as:

$$\nabla T = -\alpha g T / C_P \quad \text{(Eq. 3.3)}$$

for thermal expansion coefficient α, gravitational acceleration g, and isobaric heat capacity C_P. This equation is derived from the Adams-Williamson equation and principles of thermodynamics, including the Maxwell identities and constant entropy for an adiabatic process (Stacey & Davis, 2008).

Because thermal conductivity varies with pressure, an estimate of the pressure at the core-mantle boundary of Vesta is needed. To calculate this pressure, we use the Universal Law of Gravitation and approximate Vesta as a radially symmetric sphere with two discrete regions—the mantle and the core—in hydrostatic equilibrium to find:

$$P = - \int_{CMB}^{surface} \rho^*(r) * g(r) \, dr \quad \text{(Eq. 3.4)}$$

where ρ* is density. The *Dawn* Mission showed that for Vesta, $r = 2.63 * 10^5 \, m$ at the surface and $r = 1.1 * 10^5 \, m$ at the CMB (Russell *et al*., 2012). Using the estimates for Vesta $\rho^*_{mantle} = 3.4 \, g/cm^3$ and $\rho^*_{core} = 7.9 \, g/cm^3$ (Dreibus *et al.*, 1997) as minima and $4.0 \, g/cm^3$ and $9.0 \, g/cm^3$, respectively, as maxima, the pressure at the Vestan CMB is estimated as 0.1-0.2 GPa. At Vesta's center, the pressure is about double that of the CMB, with a central pressure estimated as 0.2-0.3 GPa. The experimental pressures are within an order of magnitude of the pressure at Vesta's CMB—and three orders of magnitude closer to Vesta's CMB pressure than atmospheric pressure on Earth is.

Therefore, our data can be extrapolated to estimate the electrical resistivity in the early Vestan core.

For estimating the adiabatic heat flux at the top of ancient Vesta's core, we extrapolate the thermal conductivity value to 0.2 GPa using the thermal conductivity values at each pressure just after melting: (2 GPa, 31.6 W/m/K), (3 GPa, 32.9 W/m/K), (4 GPa, 35.3 W/m/K), (5 GPa, 35.7 W/m/K). Graphically, these are the local minima in thermal conductivity after the melt. This gives κ = 29.1 W/m/K at 0.2 GPa. Using this value for κ in Eq. 2 along with a calculated value of T-gradient using Eq. 3 and estimates of $\alpha = 10^{-4} \, K^{-1}$ and $C_P = 800 \, J \, kg^{-1}K^{-1}$ from Weiss *et al.* (2010), and values of $g = 0.3 \, \text{m/s}^2$ and $T = 1700 \, K$, gives an adiabatic heat flux density of ~2 mW/m². (See Table 3.3)

Table 3.3: A summary of the values used to estimate adiabatic heat flux density at the top of early Vesta's core

Variable	Symbol	Estimate	Source
Thermal Expansion	α	.0001 K^{-1}	Weiss *et al.*, 2010
Heat Capacity	C	800 J K^{-1} kg^{-1}	Weiss *et al.*, 2010
Gravitational Acceleration	g	0.3 m/s^2	Calculations
Temperature	T	1700 K	This Study
Core Radius	r	110 km	Russell *et al.*, 2012

Thermal Conductivity	κ	29.1 W m^{-1} K^{-1}	This Study

Assuming radial symmetry, the total adiabatic heat flux at the top of the core at radius $r = 110$ km is $Q_{ad} = -4\pi r^2 \, \kappa \, \nabla T$ (where an estimated value of the T-gradient is derived from Eq. 3) which gives an estimated heat flux of ~300 MW. At somewhat lower pressures than these, both the thermal conductivity and the thermal gradient would be smaller and therefore, our estimates of heat flux are an upper bound.

To apply our results to the early Vestan dynamo, an estimate of the heat flux across the early Vestan CMB is needed. Weiss *et al*. (2010) estimated the heat flux density at the surface of the metallic core of Vesta before possible crystallization of the core as 500 mW/m^2, assuming that $dT/dt = 100 \, K/My$ at the top of the core. Formisano *et al*. (2016) estimate a much smaller peak heat flux density of 10 mW/m^2. These data and estimates allow for an estimate of the heat flux due to thermal convection in Vesta's early liquid core. The estimated range of values of heat flux density across early Vesta's CMB of 10-500 mW/m^2, corresponding to a heat flow of ~1.5 – 78 GW, is much greater than the adiabatic heat flux density at the top of early Vesta's core of ~2 mW/m^2, corresponding to a heat flow of ~ 300 MW, found in this study. Therefore, we conclude that even within the large uncertainties of the estimated heat flux across the CMB, the large difference in calculated adiabatic heat flux of between 0.5% and 25% of the estimated heat flux across the CMB, that thermal convection would have been an important energy source of dynamo action that generated a surface magnetic field for tens of millions of years in Vesta's early history. Even considering a heat flux density across early Vesta's CMB with a peak of only 10 mW/m^2, thermal convection would have been required to transport ~8 mW/m^2 in addition to the conducted heat component. Additionally, the study by Formisano *et al*. (2016) was based on an estimated core thermal conductivity of 40 W/m/K, which is somewhat higher than the value determined from the experiments in this study. Modifying this assumed thermal conductivity gives larger values for convective forces in the core at any point in time. This may imply that

the actual duration of the active core dynamo lies on the higher side of their estimation of 150-500 Myr, but the effect of electrical conductivity on predictions of the critical magnetic Reynolds number for dynamo formation must also be considered.

A final requirement for the generation of a dynamo is that the magnetic Reynolds number exceeds a critical value. For ideal motion in a sphere, this number is π^2 (Backus, 1958). The magnetic Reynolds number determines whether the magneto-hydrodynamic induction effect is sustained in excess of diffusive (i.e. resistive) losses (e.g., Formisano *et al.*, 2016; Weiss *et al.,* 2010). For values below the critical value, the magnetic field dissipates nearly instantly on a geological time scale because the characteristic timescale for thermal diffusion within Vesta is less than 1000 years (Stevenson, 2010). For magnetic permeability μ, characteristic core fluid velocity U, electrical conductivity σ, and characteristic length scale of fluid flow, L, which in this case can be approximated as the core radius the magnetic Reynolds number $Re_m = \sigma\mu UL$. The estimates by Weiss *et al.* (2010) use a value for σ of $6 \times 10^5 \ S/m$ (Secco and Schloessin, 1989) for pure Fe that is somewhat smaller than the value of $7 - 8.3 \times 10^5 \ S/m$ for Fe10Ni measured in our study. For the same characteristic velocity, using our value of electrical conductivity of Fe10Ni indicates Vesta's early core had a higher magnetic Reynolds number if it had a substantial amount of Ni, which is likely (e.g., Dreibus *et al*., 1997). However, because an increased electrical conductivity correlates with less stirring by thermal convection due to higher thermal conductivity and a higher conductive heat flux, the effect of an increase in electrical conductivity may be accompanied and counterbalanced by a decrease in characteristic fluid velocity. However, in cases when the characteristic fluid velocity of Vesta's core is mostly due to a process unrelated to heat transfer, the effect of Ni on the magnetic Reynolds number would be an increase relative to pure Fe. In non-thermal models of Vesta's internal dynamo that assume a composition of pure Fe, the likelihood and duration of an internal dynamo forming is somewhat greater, given our higher estimate of electrical conductivity.

3.4   Conclusions

Electrical resistivity of Fe10Ni decreases with pressure and increases with temperature. The effect of Ni on pure liquid Fe is to reduce the electrical resistivity, although this reduction is not large at high temperatures. The presence of 10wt% Ni gives a higher thermal and electrical conductivity than pure Fe-based estimates for its core composition. Even with this finding, because our estimate of ~2 mW/m^2 for the adiabatic heat flux density at the top of early Vesta's core is much smaller than estimates of heat flux density across early Vesta's CMB, early Vesta's dynamo could have been driven by thermal convection alone.

References

Backus, G. 1958. A class of self-sustaining dissipative spherical dynamos. *Annals of Physics*. 4: 372-447.

Binzel, R.P., and Xu, S. 1993. Chips off of Asteroid 4 Vesta: Evidence for the Parent Body of Basaltic Achondrite Meteorites. *Science*. 260: 186-191.

Bushby, P.J., Käpylä, P.J., Masada, Y., Brandenburg, A., Favier, B., Guervilly, C., Käpylä, M.J. 2018. Large-scale dynamos in rapidly rotating plane layer convection. *Astronomy and Astrophysics (Berlin)*. 612: A97.

Busse, F. 1970. Thermal instabilities in rapidly rotating systems. *Journal of Fluid Mechanics*. 44: 441-460.

Consolmagno, G.J., and Drake, M.J. 1977. Composition and evolution of the eucrite parent body: evidence from rare earth elements. *Geochimica et Cosmochimica Acta*. 41: 1271-1282.

Dreibus, G., Bruckner, J., Wanke, H. 1997. On the Core Mass of the Asteroid Vesta. *Meteoritics & Planetary Science*. 32: A36.

Driscoll, P.E., and Du, Z. 2019. Geodynamo Conductivity Limits. *Geophysical Research Letters*. 46, 7982-7989.

Ezenwa, I.C., and Secco, R.A. 2017. Constant electrical resistivity of Zn along the melting boundary up to 5 GPa. *High Pressure Research.* 37: 313-333.

Formisano, M., Federico, C., De Angelis, S., De Sanctis, M.C., Magni, G. 2016. A core dynamo in Vesta? *Monthly Notices of the Royal Astronomical Society*. 458: 695-707.

Fu, R.R., Weiss, B.P., Shuster, D.L., Gattacceca, J., Grove, T.L., Suavet, C., Lima, E.A., Luyao, L., Kuan, A.T. 2012. An Ancient Core Dynamo in Ancient Vesta. *Science*. 338: 238-241.

Glatzmaier, G.A., and Roberts, P.H. 1996. An anelastic evolutionary geodynamo simulation driven by compositional and thermal convection. *Physica D.* 97: 81-94.

Gomi, H., and Yoshino, T. 2019. Resistivity, Seebeck coefficient, and thermal conductivity of platinum at high pressure and temperature. *Physical Review B*. 100: 214302.

Klemens, P.G., and Williams, R.K. 1986. Thermal conductivity of metals and alloys. *International Metals Reviews*. 31: 197-215.

Konopliv, A.S., Asmar, S.W., Bills, B.G., Mastrodemos, N., Park, R.S., Raymond, C.A., Smith, D.E., Zuber, M.T. 2011. The Dawn Gravity Investigation at Vesta and Ceres. *Space Science Review*. 163: 461-486.

Larmor, J. 1919. Possible Rotational Origin of Magnetic Fields of Sun and Earth. *Engineering Review*. 108: 461ff.

Littleton, J.A.H., Secco, R.A., Yong, W. 2018. Decreasing electrical resistivity of silver along the melting boundary up to 5 GPa. *High Press Research.* 38: 99-106.

McCord, T.B., Adams, J.B., Johnson, T.V. 1970. Asteroid Vesta: Spectral Reflectivity and Compositional Implications. *Science*. 168: 1445-1447.

Nimmo, F. 2009. Energetics of asteroid dynamos and the role of compositional convection. *Geophysical Research Letters*. 36: 1-6.

O'Brien, D.P., and Sykes, M.V. 2011. The Origin and Evolution of the Asteroid Belt—Implications for Vesta and Ceres. *Space Science Reviews.* 163, 41-61.

Pommier, A., Davies, C.J., Zhang, R. 2020. A Joint Experimental-Modeling Investigation of the Effect of Light Elements on Dynamos in Small Planets and Moons. *Journal of Geophysical Research: Planets*. 125: p. n/a.

Roberts, P.H. 1968. On the thermal instability of a rotating-fluid sphere containing sources. *Philosophical Transactions for the Royal Society of London. Series A, Mathematical and Physical Sciences*. 263: 93-117.

Russell, C.T., Raymond, C.A., Coradini, A., McSween, H.Y., Zuber, M.T., Nathues, A., De Sanctis, M.C., Jaumann, R., Konopliv, A.S., Preusker, F., Asmar, S.W., Park, R.S., Gaskell, R., Keller, H.U., Mottola, S., Roatsch, T., Scully, J.E.C., Smith, D.E., Tricarico, P., Toplis, M.J., Christensen, U.R., Feldman, W.C., Lawrence, D.J., McCoy, T.J., Prettyman, T.H., Reedy, R.C., Sykes, M.E., Titus, T.N. 2012. Dawn at Vesta: Testing the Protoplanetary Paradigm. *Science.* 336: 684-686.

Secco, R.A. 1995. High *p, T* physical property studies of Earth's interior: thermoelectric power of solid and liquid Fe up to 6.4 GPa. *Canadian Journal of Physics.* 73: 287–294.

Secco, R.A., and Schloessin, H.H. 1989. The electrical resistivity of solid and liquid Fe at pressures up to 7 GPa. *Journal of Geophysical Research: Solid Earth*. 94: 5887-5894.

Silber, R.E., Secco, R.A., Yong, W. 2017. Constant electrical resistivity of Ni along the melting boundary up to 9 GPa. *Journal of Geophysical Research: Solid Earth*. 122: 5064-5081.

Silber, R.E., Secco, R.A., Yong, W., Littleton, J.A.H. 2018. Electrical resistivity of liquid Fe to 12 GPa: Implications for heat flow in cores of terrestrial bodies. *Scientific Reports*. 8: 10758-9.

Stacey, F.D., and Davis, P.M., 2008. *Physics of the Earth.* Cambridge University Press. p. 326

Stevenson, D.J. 2010. Planetary Magnetic Fields: Achievements and Prospects. *Space Science Reviews.* 152: 651-664.

Vernazza, P., Brunetto, R., Strazzulla, G., Fulchignoni, M., Rochette, P., Meyer-Vernet, N., Zouganelis, I. 2006. Asteroid colors: a novel tool for magnetic field detection? The case of Vesta. *Astronomy & Astrophysics*. 451: L43-L46.

Wasson, J.T., 2013. Vesta and extensively melted asteroids: Why HED meteorites are probably not from Vesta. *Earth and Planetary Science Letters*. 381: 138-146.

Weiss, B.P., Gattacceca, J., Stanley, S., Rochette, P., Christensen, U.R. 2010. Paleomagnetic Records of Meteorites and Early Planetesimal Differentiation. *Space Science Reviews*. 152: 341-390.

Wiedemann, D. and Franz, R. 1853. Uber die Warme-Leitungfahligkeit der Metalle. *Annalen der Physik.* 165: 497-531.

Williams, Q. 2009. Bottom-up versus top-down solidification of the cores of small solar system bodies: Constraints on paradoxical cores. *Earth and Planetary Science Letters.* 284: 564-569.

Chapter 4

4   Conclusion

4.1   Summary

The electrical resistivity of Fe10Ni was measured from 2-5 GPa and up to at most 2082 K using a 1000-ton cubic anvil press. Electron microprobe results show little contamination up to and near melting. As expected, the electrical resistivity of Fe10Ni increases monotonically with temperature. Sudden changes in slope occur at two temperatures: ~800 K and ~1700 K. The former corresponds to the transition from a bcc (α) structure to an fcc (γ) structure, while the latter corresponds to melting.

These electrical resistivity measurements were used to calculate the thermal conductivity of Fe10Ni at the same pressures and temperatures. Within the temperature range measured, the maximum thermal conductivity at each pressure corresponded to the melting temperature, while the minimum thermal conductivity at each pressure corresponded to the transition from a bcc (α) structure to an fcc (γ) structure. Between these two points, thermal conductivity increases monotonically.

These results provide insight into the thermal evolution of the asteroid Vesta. Using thermal conductivity values, the calculated adiabatic heat flux at the top of early Vestan core was estimated as ~300 MW. Compared to pure Fe-based estimates for a Vestan core composition, the presence of 10wt% Ni gives a slightly lower electrical resistivity and higher thermal conductivity. However, because our estimates of the adiabatic heat flux density at the top of early Vesta's core is much smaller than estimates of heat flux density across early Vesta's CMB, early Vesta's dynamo could have been driven by thermal convection alone even with the presence of 10wt% Ni. These results may also have implications for dynamo action in any other small, differentiated bodies in the early solar system.

4.2   Suggestions for Future Research

Further high-pressure resistivity experiments could be performed on Fe-Ni alloys in the liquid state. For example, because the experiments in this study found the behavior at high temperatures of Fe10Ni to be nearer to pure Fe than expected, future studies could further examine the effect of Ni, such as in various weight percentages, on Fe resistivity near melting temperatures with experimental and theoretical approaches. One problem arising from experimental methods that could potentially be resolved is the extensive contamination of the sample after ~100 K above the melting temperature. At higher pressures than Fe10Ni has ever been studied, nearing 1 TPa, experiments on Fe10Ni in the liquid state could have important implications for the dynamo formation in super-Earth exoplanets.

Furthermore, various ternary systems such as Fe-Ni-Si, Fe-Ni-S, and Fe-Ni-Co should be studied at high pressures. While Ni has a lower electrical resistivity of Fe, light elements generally have a higher electrical resistivity—these elements acting in combination in high-pressure resistivity experiments could yield interesting results that are more mimetic of core compositions than binary systems are. These experiments could be used to draw conclusions about heat flow through the cores of terrestrial planetary bodies of the chosen composition, temperature, and pressure.

Appendices

Appendix A: Additional Details on Methods

A.1 Cubic Cell Design

For transmitting pressure from the 1000-ton cubic anvil press onto a given sample, a cubic pressure cell was constructed. The cell consisted primarily of a 31.75 mm pyrophyllite ($Al_4Si_8O_{20}OH_4$) cube (see **Error! Reference source not found.** with a 10.7-mm diameter cylindrical hole bored through the middle. This hole was filled with sleeves (cylindrical annuli, see Figure A 2) of various materials as described below, which collectively encapsulated the iron-nickel sample at the center. For ease of construction, this cube was cut along the cross-section of the cylindrical hole into three pieces. To reassemble these three pieces accurately, two 5.08-mm diameter holes coaxial with the large hole were cut at the same point near the corner in each of the three pieces. A continuous pyrophyllite cylinder was used as a pin and was placed in each hole in order to hold the three pieces of the cube together.
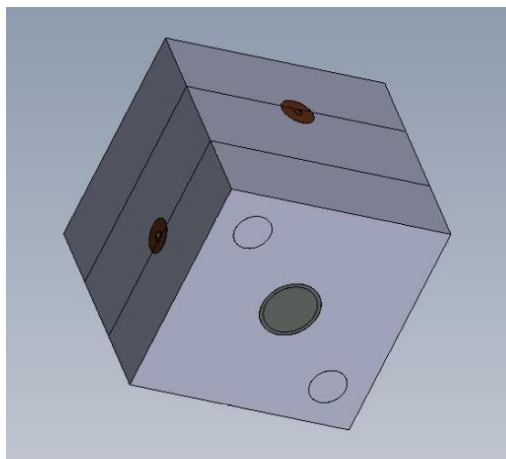
Figure A 1: A drawing of the cubic pressure cell with edges of 31.75 mm, created in SOLIDWORKS© software package
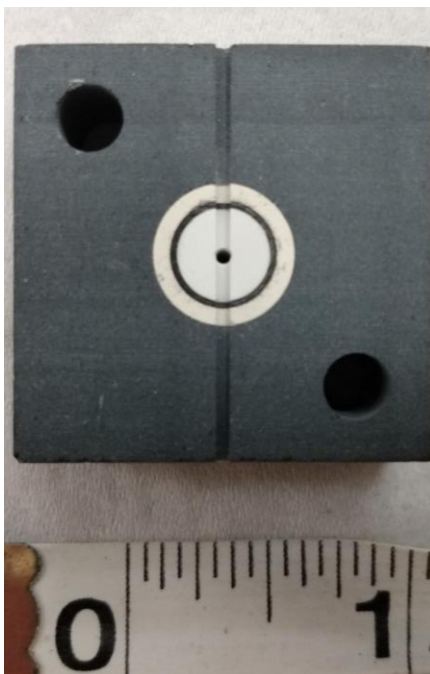
Figure A 2: The central third of three slabs of a cubic pressure cell, with inch scale and groove for wires

The materials comprising the 102-mm length cylindrical sleeves included boron nitride (BN), Ceramic (Al_2O_3), Zirconia (ZrO_2), and Graphite (C). Thicknesses given here are approximate and were varied from cube to cube. The boron nitride sleeve (7 mm outer diameter) was emplaced in the center with the purpose of containing the liquid sample as it melted. The three graphite sleeves (0.5 mm thickness) and two outer caps (see Figure A 3) functioned as a furnace. The graphite parts (e.g., Figure A 4) physically contacted continuously from the top to the bottom of the cube and transmitted heat into the interior of the cell when electrical current was passed through them. Surrounding the middle third of this graphite sleeve was a sleeve (2.5 mm thickness) made of zirconia (see Figure A 5) for thermal insulation. Two zirconia caps were also placed inside the graphite furnace, enclosing the middle third of the interior.
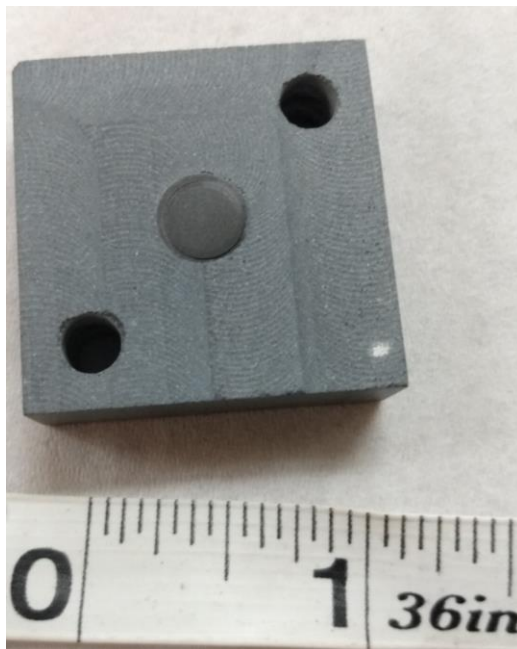
Figure A 3: Outer slab of pyrophyllite cube, showing the graphite cap and cylinder used for heating

Figure A 4: The reverse side of the slab in Figure A 3 with recessed space where zirconia disk will be emplaced for thermally insulating sample

Figure A 5: Zirconia cylinder before turning on a lathe, with inch scale

At the center of each cube (see Figure A 6), the wire sample (Fe10Ni) was placed inside a ceramic tube, which was placed in the boron nitride sleeve. Additionally, two thermocouples were placed next to the sample to measure temperature as a function of voltage difference. These thermocouples consisted simply of Type C wires (W5%Re and W26%Re) crossed over themselves to form a pressure-welded junction. The wire was insulated inside a ceramic tube with four parallel holes.
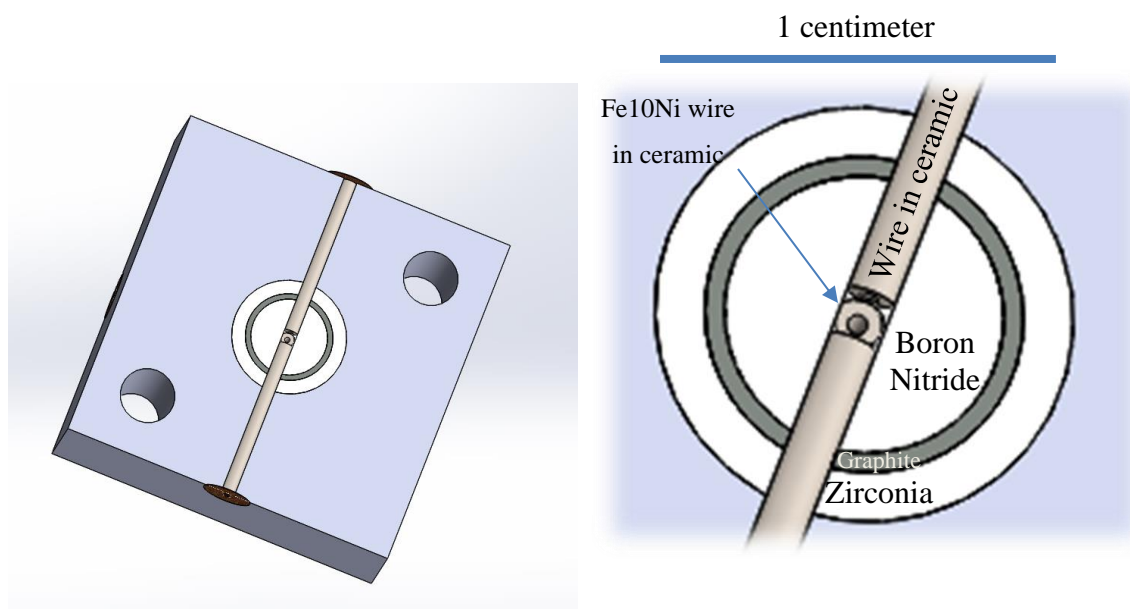
Figure A 6: A drawing of the central third of the cubic pressure cell, with a central zoom-in, created in SOLIDWORKS© software package

A.2 The Press

The experiments were carried out on a large-volume 1000-ton cubic anvil press (see Figure A 7). Previously, this press had been pressure-calibrated at both room and high temperatures. Each anvil was hydraulically driven to exert quasi-hydrostatic pressure symmetrically on the small cubic pressure cell. To increase friction between the pressure cell and the anvil faces, forming a gasket, the pyrophyllite surface of the cube was painted red with Fe_2O_3. The six anvil faces then compressed in three mutually orthogonal directions, with one opposing pair of faces used for heating the graphite annulus and the other two pairs used for the four-wire technique of measurement. Copper tabs (see Figure A 8) on four faces of the cube ensured electrical contact between the respective wire and anvil face.
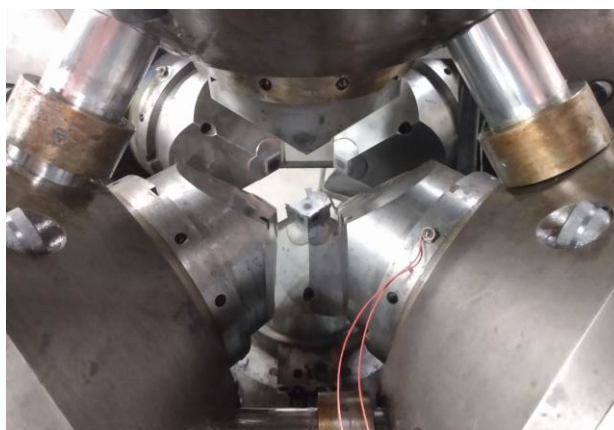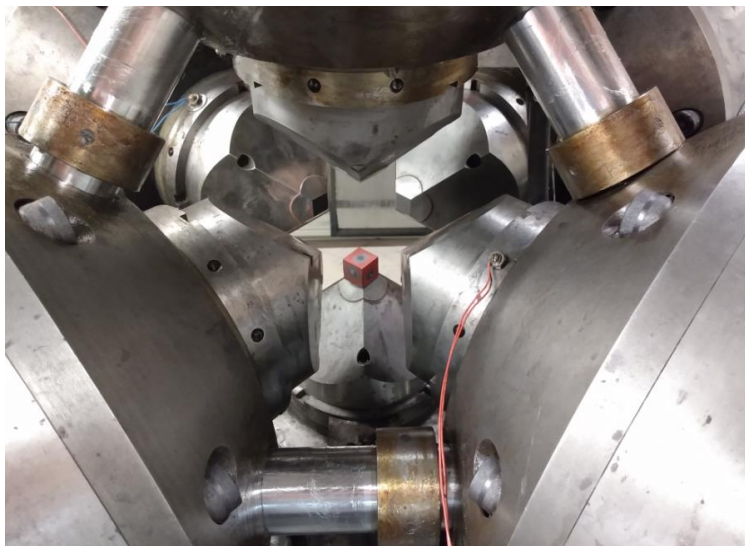
Figure A 7: The press and pressure cell pre-experiment (upper) and post-experiment (lower). For scale, the pre-experimental cube (red) has edge length of 31.8 mm, while the post-experimental cube has edge length of 25.4 mm.

Figure A 8: A post-experimental cubic pressure cell, edge length of ~25 mm

A.3 4-Wire Method of Electrical Resistivity Measurement

To allow for the 4-wire method of measuring resistance, Type C wires (W5%Re and W26%Re) were placed in each cell. In this method, the wires connect a current and a voltage electrode to each side of the sample to a voltmeter and a power source as well as cross over each other, forming a thermocouple. These thermocouples each contacted the side of a thin Pt disk which contacted each end of the sample. A long, thin ceramic tube manufactured with four coaxial holes housed the wires connecting from the power source to the sample and back, as well as from the voltmeter to the sample and back. Each resistivity data point presented as results for a certain temperature is derived from the average of several measurements (depending on time spent at that temperature) by the voltmeter with a resolution of 1 μV.

A.4 Individual Experimental Runs

Table A 1: The pressure and peak temperature of experimental runs in this study

Run Number	Pressure (GPa)	Peak Temperature (K)

1	4	~2000
2	4	~1700
3	4	~1900
4	5	~1000
5	5	2082
6	5	1729
7	5	1820
8	4	2035
9	5	1780
10	3	1941
11	4	2000
12	3	1969
13	2	1706
14	2	1869
15	2	1897
16	5	1853

Appendix B: Additional EMPA and Resistivity Results

B.1   EMPA Results

The following sample (Fig A1) was recovered from approximately 60 K below melting. For points 5-16, note the closeness to the starting composition of 10wt% Ni and 90wt% Fe:
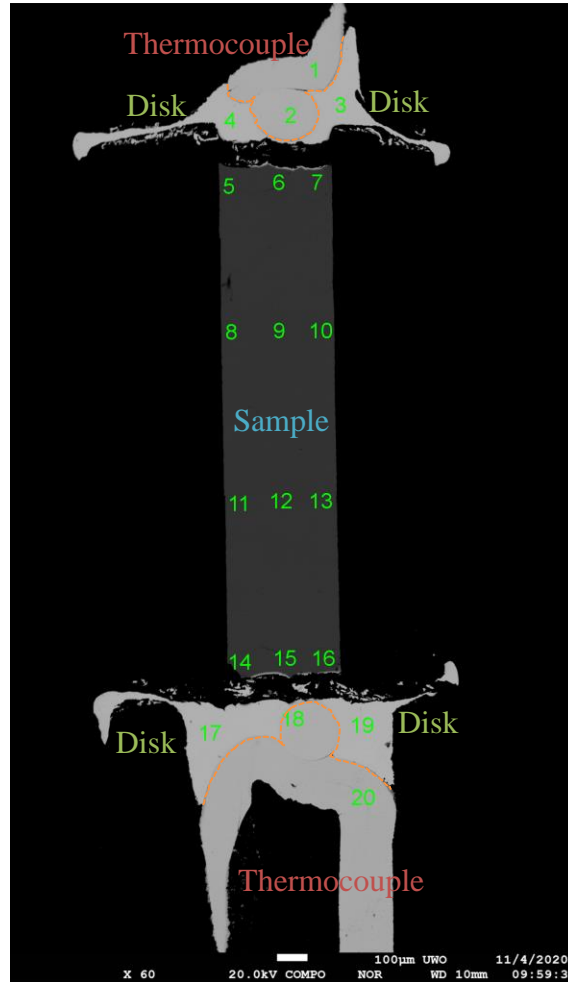
Figure B 1: Fe10Ni sample recovered from 1729 K and 5 GPa

Table B 1: Composition of sample in Figure B 1 from EMPA

Point	Fe(wt%)	Ni(wt%)	Pt(wt%)	W(wt%)	Re(wt%)	Total(wt%)
1	0.008	0.031	0.33	94.829	4.572	99.77
2	nd	0.002	0.208	73.871	25.643	99.724
3	0.009	nd	100.421	nd	nd	100.43

4	0.012	0.003	99.61	nd	nd	99.625
5	89.951	9.705	nd	nd	nd	99.656
6	90.098	9.626	0.014	nd	nd	99.738
7	90.852	9.534	nd	nd	nd	100.386
8	90.358	9.545	nd	nd	nd	99.903
9	90.106	9.682	nd	nd	nd	99.788
10	90.253	9.683	nd	nd	nd	99.936
11	90.014	9.718	nd	nd	nd	99.732
12	90.365	9.729	0.006	nd	nd	100.1
13	90.473	9.743	nd	nd	nd	100.216
14	89.688	9.488	nd	nd	nd	99.176
15	90.158	9.537	0.026	nd	nd	99.721
16	89.963	9.653	0.006	nd	nd	99.622
17	nd	nd	100.392	nd	nd	100.392
18	0.005	0.031	0.288	74.184	25.482	99.99
19	nd	nd	100.289	nd	nd	100.289
20	0.012	0.045	0.259	94.73	4.72	99.766
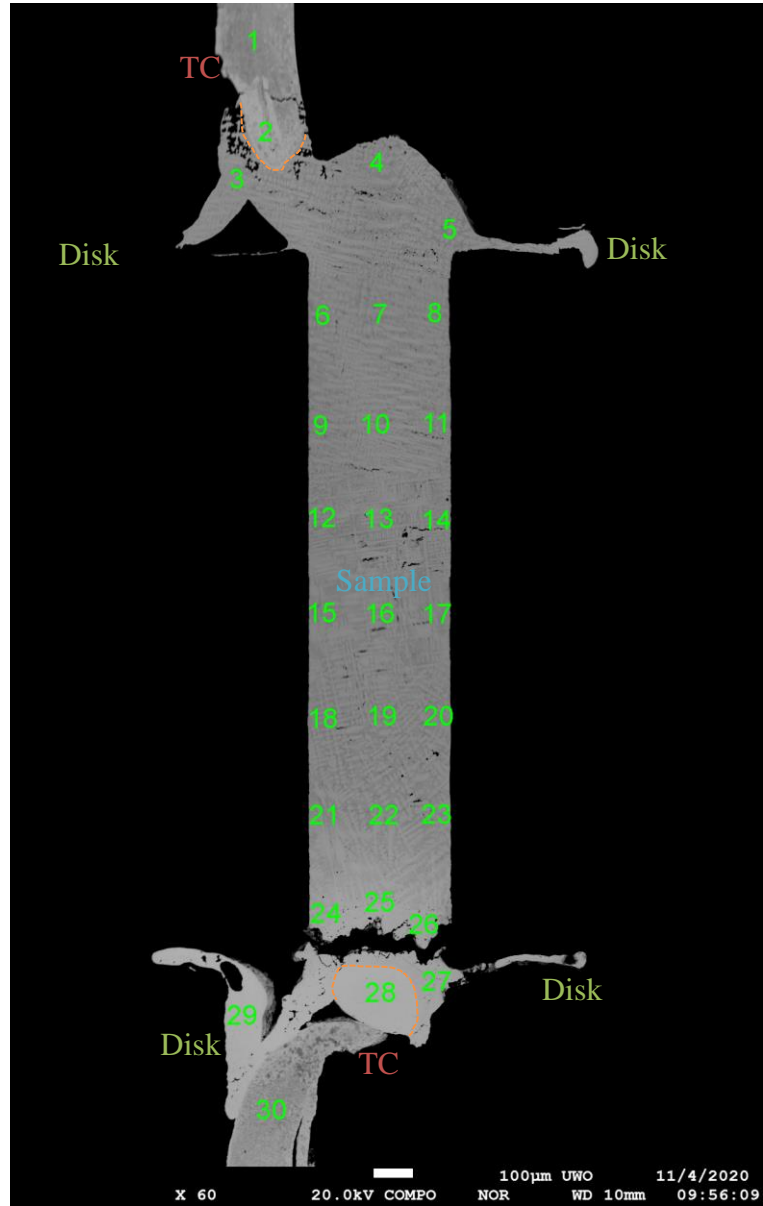
Figure B 2: Fe10Ni sample recovered from 2082 K and 5 GPa

Table B 2: Composition of sample in Figure B 2 from EMPA

Point	Fe(wt%)	Ni(wt%)	Pt(wt%)	W(wt%)	Re(wt%)	Total(wt%)
1	nd	0.04	0.298	89.16	4.142	93.64
2	nd	0.053	0.296	91.574	4.376	96.299
3	30.7	3.815	47.044	15.488	1.495	98.542
4	32.575	3.301	41.339	18.507	3.328	99.05
5	31.43	3.295	37.994	22.833	3.478	99.03
6	34.446	3.682	44.214	14.698	2.185	99.225

7	32.643	3.153	44.655	15.801	2.976	99.228
8	34.294	3.567	40.437	17.335	2.935	98.568
9	35.673	3.894	42.464	15.016	2.482	99.529
10	32.37	3.514	39.464	20.965	3.637	99.95
11	33.214	3.455	39.452	18.208	3.259	97.588
12	36.958	4.146	43.072	13.483	2.551	100.21
13	33.238	3.521	41.671	17.589	3.448	99.467
14	36.267	4.134	38.874	16.088	2.815	98.178
15	36.495	4.134	42.098	13.193	2.772	98.692
16	33.228	3.498	42.432	16.423	3.515	99.096
17	36.533	4.083	42.244	13.333	2.881	99.074
18	35.729	3.876	43.684	13.329	3.007	99.625
19	35.863	4.089	40.017	15.815	3.017	98.801
20	34.161	3.431	44.972	12.918	3.532	99.014
21	32.021	3.744	53.043	8.787	1.855	99.45
22	30.552	3.451	50.001	12.096	3.039	99.139
23	29.935	3.045	50.966	11.58	3.18	98.706
24	16.617	1.692	75.095	5.175	1.332	99.911
25	16.869	1.731	76.697	3.076	0.591	98.964
26	20.19	2.873	73.677	1.249	0.21	98.199
27	13.002	1.284	81.244	3.999	0.853	100.382
28	0.004	0.029	0.252	74.316	24.764	99.365
29	3.786	0.349	94.271	0.731	0.105	99.242
30	nd	0.043	0.277	91.521	4.26	96.101
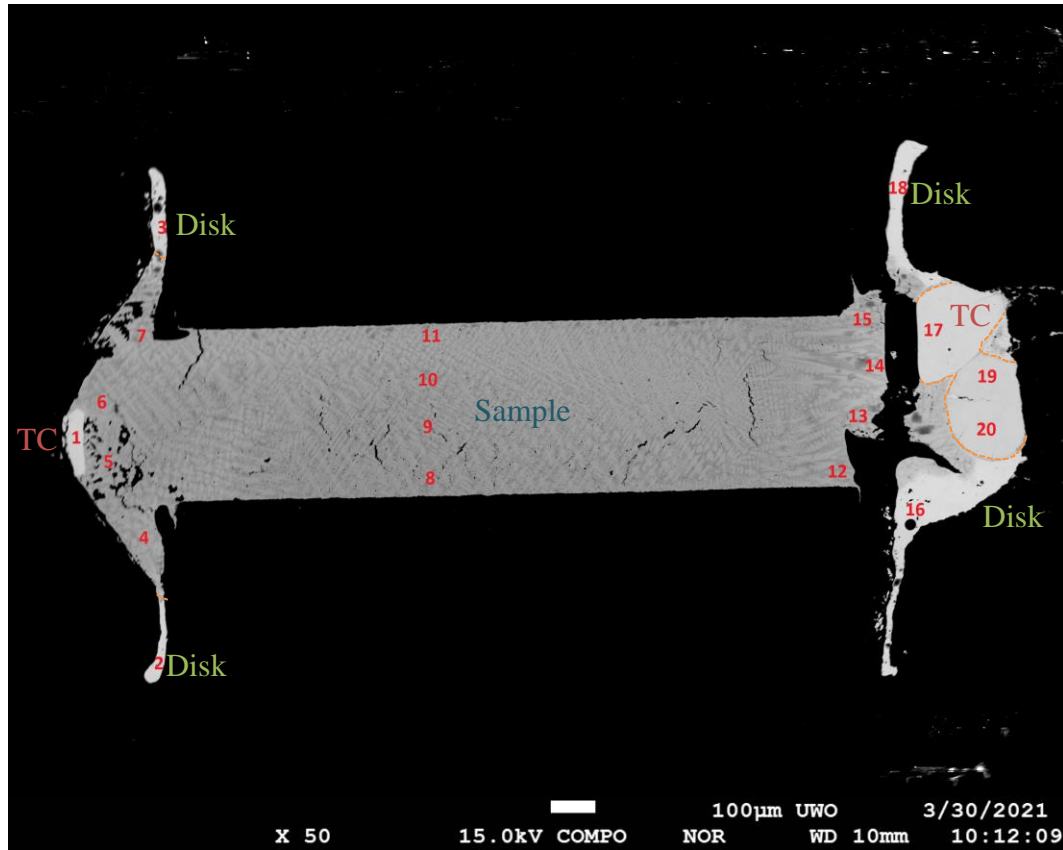
Figure B 3: Fe10Ni sample recovered from 2000 K and 4 GPa

Table B 3: Composition of sample in Figure B 3 from EMPA

Point	Fe(wt%)	Re(wt%)	Pt(wt%)	Ni(wt%)	W(wt%)	Total(wt%)
1	0.065	3.86	0.334	0.034	93.271	97.564
2	1.584	nd	89.065	0.129	1.324	92.102
3	4.301	0.049	92.672	0.307	0.373	97.702
4	35.634	2.303	38.911	4.472	16.614	97.934
5	33.537	3.77	36.766	3.447	19.587	97.107
6	33.18	4.359	37.075	3.522	20.37	98.506
7	33.194	3.901	39.2	3.703	18.046	98.044
8	40.892	3.274	37.463	4.483	13.053	99.165
9	40.566	2.877	35.326	4.736	14.472	97.977
10	37.091	3.069	37.305	4.172	15.178	96.815
11	32.073	3.216	41.507	3.368	16.21	96.374
12	32	4.069	47.883	3.035	11.384	98.371

13	36.35	1.666	44.118	4.925	10.068	97.127
14	27.996	3.488	49.247	3.083	12.996	96.81
15	30.494	3.122	47.09	3.669	12.401	96.776
16	1.092	0.025	94.575	0.057	0.039	95.788
17	0.014	24.647	0.257	nd	72.799	97.717
18	0.125	nd	97.212	nd	nd	97.337
19	0.009	3.85	0.3	0	92.925	97.084
20	0.008	4.034	0.342	0.023	91.737	96.144
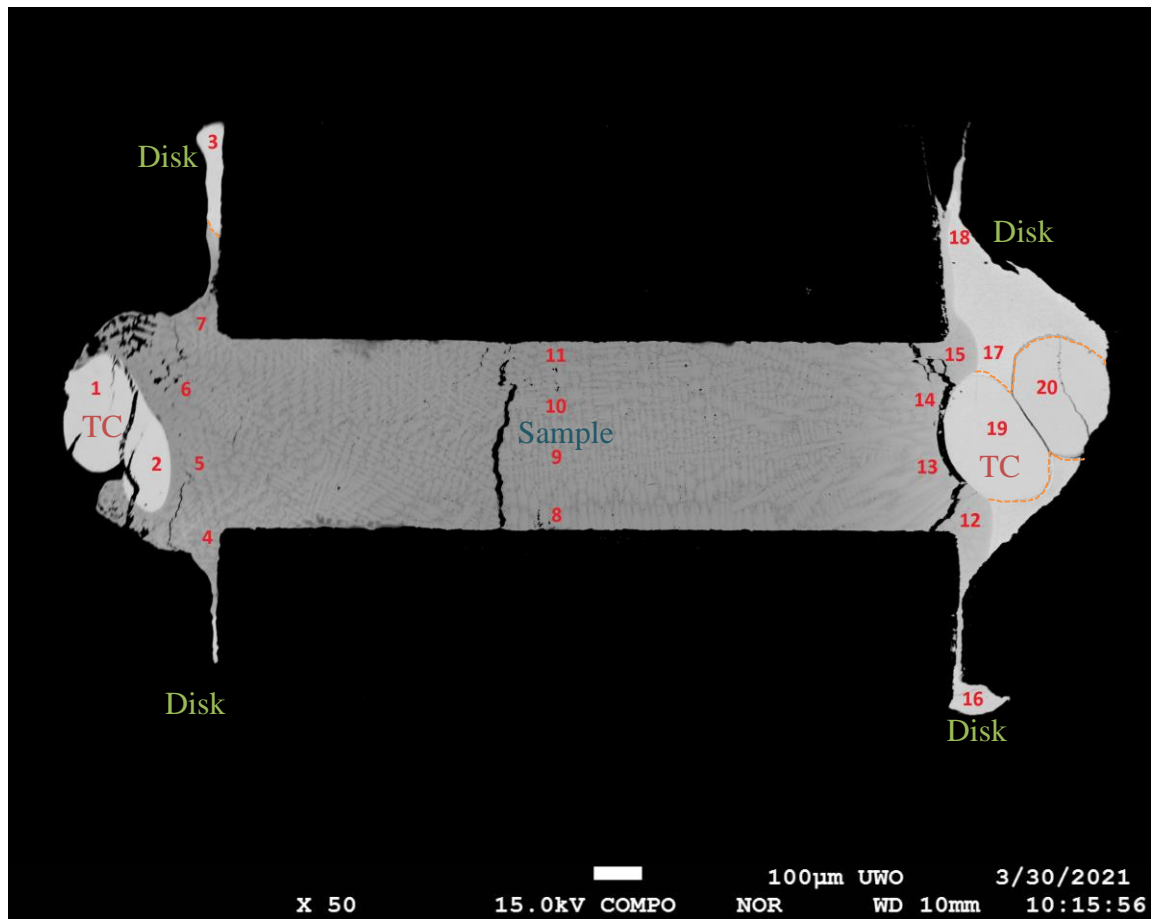
Figure B 4: Fe10Ni sample recovered from 1969 K and 3 GPa

Table B 4: Composition of sample in Figure B 4 from EMPA

Point	Fe(wt%)	Re(wt%)	Pt(wt%)	Ni(wt%)	W(wt%)	Total(wt%)
1	0.006	4.483	0.341	0.001	90.962	95.793
2	nd	24.175	0.313	nd	72.552	97.04
3	nd	0.009	95.7	0.008	nd	95.717
4	34.928	1.997	44.906	3.92	11.324	97.075

5	36.051	3.194	42.227	3.549	11.926	96.947
6	39.925	1.49	42.522	4.287	9.514	97.738
7	38.824	2.685	41.535	4.271	9.806	97.121
8	42.236	1.115	45.989	4.631	3.88	97.851
9	41.5	1.577	42.127	4.935	7.993	98.132
10	41.826	1.368	41.584	4.838	7.931	97.547
11	42.576	1.008	44.36	4.556	4.651	97.151
12	21.414	0.009	72.771	2.015	0.361	96.57
13	29.752	0.363	62.123	3.301	1.431	96.97
14	28.161	0.671	62.727	2.871	2.498	96.928
15	24.63	0.09	68.571	2.695	0.836	96.822
16	0.014	nd	88.551	nd	nd	88.565
17	0.005	nd	94.098	nd	nd	94.103
18	nd	0.014	93.058	nd	nd	93.072
19	nd	23.597	0.277	0.013	73.182	97.069
20	0.011	4.038	0.367	nd	92.048	96.464
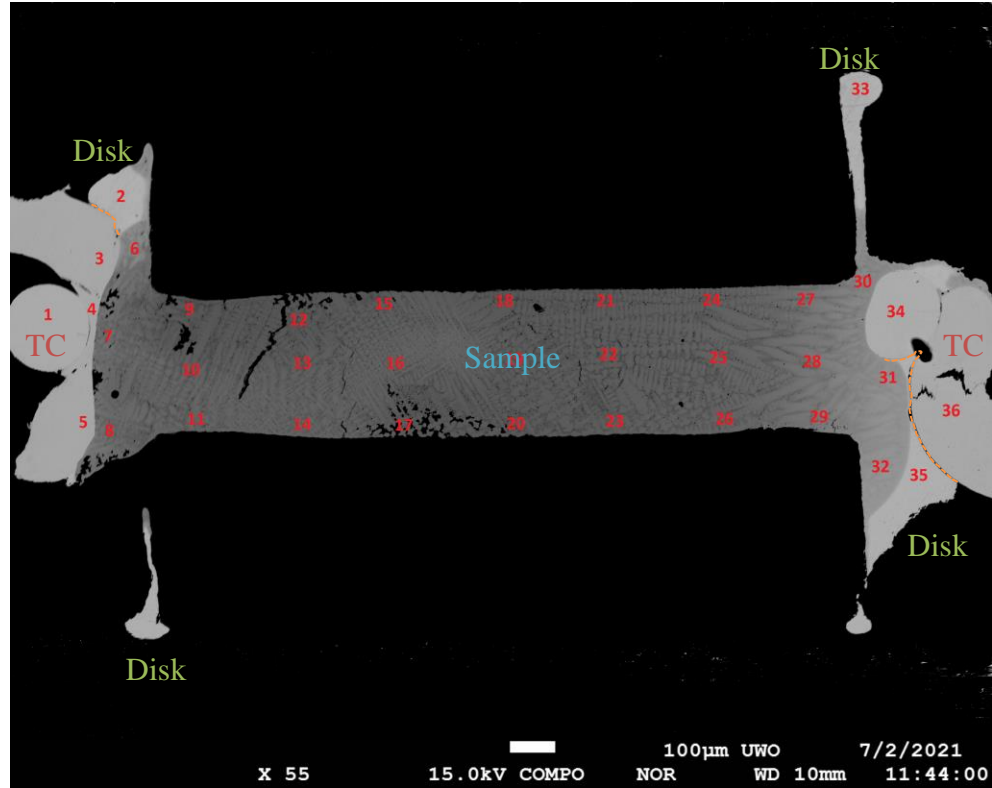
Figure B 5: Fe10Ni sample recovered from 1897 K and 2 GPa

Table B 5: Composition of sample in Figure B 5 from EMPA

Point	Fe(wt%)	Re(wt%)	Pt(wt%)	Ni(wt%)	W(wt%)	Total(wt%)
1	nd	24.814	0.191	nd	74.892	99.897
2	nd	0.015	99.811	nd	0.002	99.828
3	0.181	3.857	0.382	0.036	95.344	99.8
4	0.559	3.988	0.453	0.053	94.639	99.692
5	0.277	3.881	0.406	0.027	94.832	99.423
6	29.969	0.962	44.721	3.175	21.652	100.479
7	43.817	1.299	22.017	5.498	27.514	100.145
8	42.598	0.933	35.917	4.696	16.241	100.385
9	54.316	0.398	29.846	6.296	6.587	97.443
10	48.953	0.836	34.033	5.528	11.094	100.444
11	48.556	0.446	35.402	5.601	10.055	100.06
12	54.602	0.118	30.267	6.192	6.597	97.776
13	54.089	0.368	30.824	6.268	8.237	99.786
14	49.167	0.43	37.311	5.383	8.873	101.164
15	50.896	0.42	36.467	5.205	7.239	100.227
16	48.51	0.354	36.664	5.386	9.056	99.97

17	53.162	0.332	36.245	5.51	5.778	101.027
18	54.463	0.23	34.93	5.641	5.465	100.729
19	54.058	0.337	32.457	6.333	6.703	99.888
20	54.564	0.313	33.694	6.02	6.323	100.914
21	54.376	0.219	33.731	6.138	5.49	99.954
22	52.462	0.378	36.322	5.406	6.459	101.027
23	52.149	0.485	35.155	5.573	6.794	100.156
24	48.957	0.53	41.406	4.949	5.108	100.95
25	50.435	0.492	36.209	5.889	6.437	99.462
26	48.649	0.154	39.126	5.457	5.828	99.214
27	40.216	1.151	50.667	4.425	3.974	100.433
28	39.926	0.62	52.085	4.436	3.355	100.422
29	39.116	0.202	53.361	4.72	2.313	99.712
30	29.859	1.751	61.121	2.933	5.411	101.075
31	23.224	0.158	73.965	2.134	1.169	100.65
32	21.048	0.166	76.412	2.866	0.47	100.962
33	0.012	nd	101.5	nd	nd	101.512
34	nd	25.051	0.212	0.005	74.573	99.841
35	nd	nd	99.979	nd	nd	99.979
36	nd	3.98	0.277	nd	95.809	100.066

B.2   Resistivity Results

Table B 6: Dimensions of the samples displayed in Appendix B.1.

Pressure (GPa)	Average Length (mm) [individual measurements]	Average Diameter (mm) [individual measurements]	Experimental Run Number
5	**1.95** [1.91, 1.96, 1.96, 1.95]	**0.39** [0.39, 0.39, 0.38]	5
4	**1.94** [1.93, 1.95, 1.95, 1.93]	**0.39** [0.40, 0.40, 0.38]	11
3	**1.63** [1.62, 1.66, 1.61, 1.62]	**0.41** [0.41,0.41,0.40]	12

| 2 | **1.61** [1.62, 1.62, 1.59, 1.60] | **0.39** [0.40,0.38,0.39] | 15 |
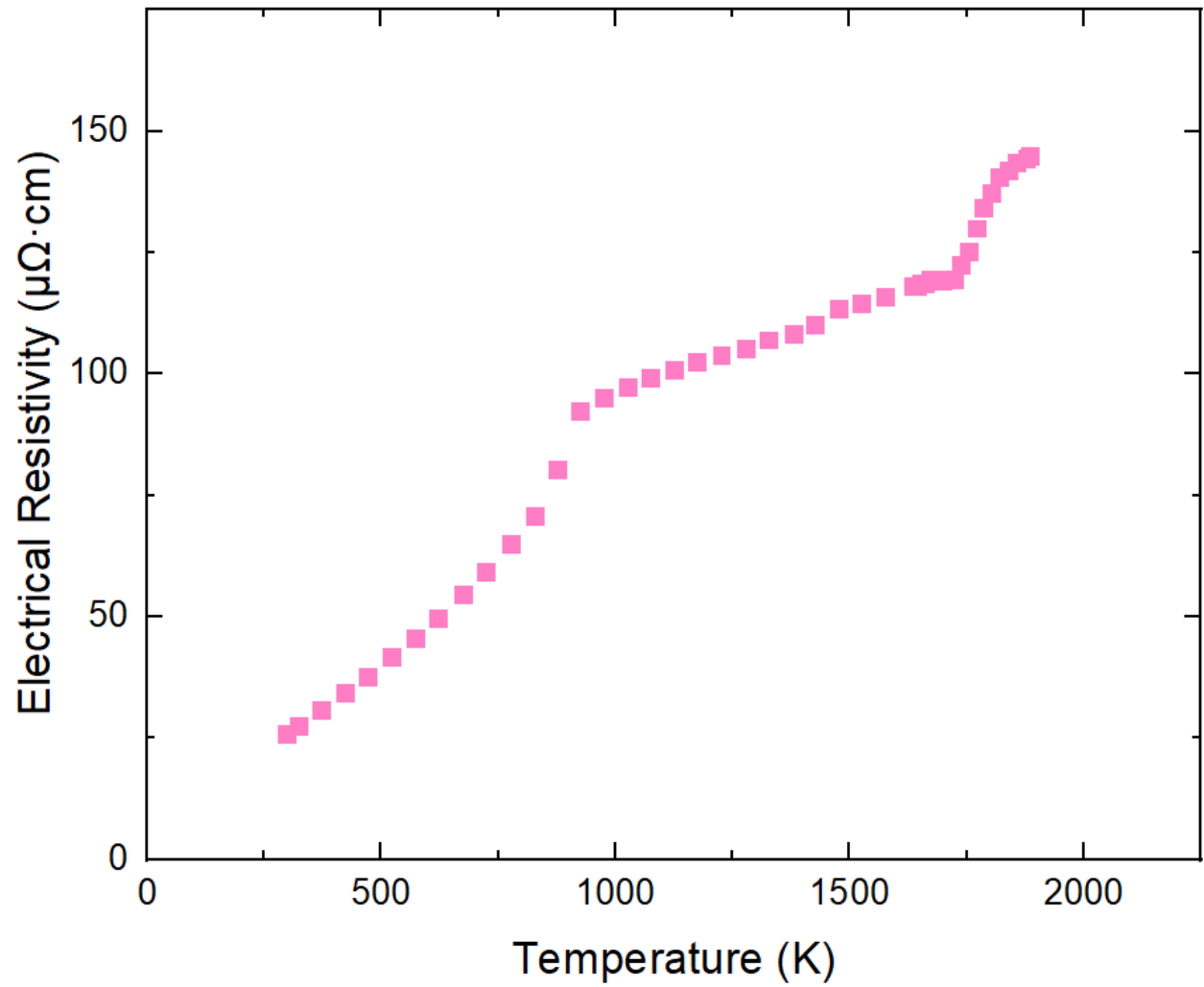
Figure B 6: Electrical resistivity of Fe10Ni at 2 GPa as a function of temperature; data in Table B 7

Table B 7: Averaged data from an experimental run (#15) at 2 GPa

Temperature (K)	Voltage (V)	Resistivity (μΩ·cm)	Resistivity (μΩ·cm) corrected for Pt	Thermal Conductivity (W/m/K)
299	0.00069	25.6	25.5	28.5
324	0.00074	27.4	27.3	29.0
373	0.00083	30.7	30.6	29.7
425	0.00092	34.3	34.1	30.4
473	0.00101	37.4	37.3	30.9
525	0.00112	41.6	41.5	30.9
575	0.00123	45.6	45.5	30.9
623	0.00134	49.5	49.4	30.8
677	0.00147	54.5	54.3	30.4
725	0.00160	59.3	59.1	29.9
778	0.00175	64.9	64.7	29.3
830	0.00191	70.8	70.6	28.7
878	0.00217	80.4	80.2	26.7
926	0.00249	92.3	92.1	24.5
977	0.00256	95.1	94.8	25.2
1028	0.00263	97.5	97.2	25.8
1078	0.00268	99.3	99.1	26.5
1128	0.00272	100.9	100.6	27.4
1176	0.00276	102.5	102.2	28.1
1228	0.00280	104.0	103.7	28.9
1281	0.00284	105.4	105.1	29.8
1329	0.00289	107.1	106.8	30.4
1382	0.00292	108.3	107.9	31.3
1428	0.00297	110.4	110.0	31.7
1479	0.00306	113.5	113.1	31.9
1525	0.00309	114.6	114.2	32.6
1579	0.00313	116.2	115.8	33.3
1637	0.00319	118.2	117.8	33.9
1645	0.00319	118.4	118.0	34.0
1653	0.00320	118.8	118.4	34.1
1663	0.00320	118.8	118.4	34.3
1675	0.00322	119.5	119.1	34.3
1687	0.00322	119.3	118.9	34.6
1699	0.00322	119.3	118.9	34.9
1712	0.00323	119.8	119.3	35.0
1726	0.00323	119.7	119.3	35.3
1740	0.00331	122.7	122.3	34.7
1755	0.00338	125.5	125.0	34.3
1772	0.00351	130.2	129.8	33.3
1788	0.00362	134.5	134.0	32.5
1805	0.00371	137.6	137.1	32.1
1822	0.00379	140.7	140.3	31.7
1841	0.00383	142.1	141.6	31.7
1859	0.00388	143.9	143.4	31.6
1879	0.00390	144.7	144.2	31.8
1887	0.00391	145.2	144.7	31.8

Table B 8: Averaged data from an experimental run (#12) at 3 GPa

Temperature (K)	Voltage (V)	Resistivity (μΩ·cm)	Resistivity (μΩ·cm) corrected for Pt	Thermal Conductivity (W/m/K)
298	0.00064	25.9	25.8	28.2
324	0.00068	27.7	27.6	28.7
375	0.00077	31.1	31.0	29.5
424	0.00085	34.5	34.4	30.1
473	0.00094	37.9	37.8	30.5
526	0.00103	41.9	41.7	30.8
575	0.00113	45.8	45.6	30.7
624	0.00124	50.0	49.9	30.5
678	0.00136	55.1	54.9	30.1
725	0.00148	59.8	59.6	29.7
776	0.00160	65.0	64.7	29.3
827	0.00178	72.0	71.8	28.1
877	0.00220	88.9	88.7	24.1
925	0.00231	93.7	93.4	24.2
977	0.00236	95.6	95.4	25.0
1027	0.00240	97.1	96.9	25.9
1079	0.00243	98.6	98.3	26.8
1127	0.00246	99.8	99.5	27.6
1176	0.00249	101.0	100.7	28.5
1229	0.00253	102.6	102.3	29.3
1276	0.00258	104.3	104.0	29.9
1323	0.00262	106.1	105.7	30.5
1374	0.00268	108.4	108.0	31.0
1425	0.00270	109.5	109.2	31.8
1476	0.00273	110.4	110.0	32.7
1524	0.00277	112.2	111.8	33.3
1574	0.00281	113.7	113.3	33.9
1585	0.00282	114.1	113.7	34.0
1590	0.00282	114.2	113.8	34.1
1596	0.00283	114.4	114.0	34.2
1603	0.00283	114.6	114.1	34.3
1618	0.00284	114.9	114.5	34.5
1626	0.00284	115.2	114.7	34.6
1636	0.00285	115.3	114.9	34.7
1646	0.00285	115.5	115.1	34.9
1657	0.00286	115.8	115.4	35.0
1668	0.00287	116.0	115.6	35.2
1679	0.00288	116.4	116.0	35.3
1691	0.00288	116.7	116.2	35.5
1704	0.00289	117.1	116.7	35.6
1718	0.00290	117.4	117.0	35.8
1734	0.00291	118.0	117.6	36.0
1749	0.00292	118.3	117.9	36.2
1766	0.00295	119.6	119.2	36.2
1781	0.00301	122.0	121.5	35.8
1798	0.00312	126.5	126.1	34.8
1816	0.00319	129.2	128.8	34.4
1837	0.00326	132.0	131.5	34.1
1859	0.00332	134.4	133.9	33.9
1880	0.00342	138.4	137.9	33.3
1902	0.00347	140.3	139.9	33.2
1929	0.00355	143.7	143.2	32.9
1955	0.00359	145.3	144.8	32.9
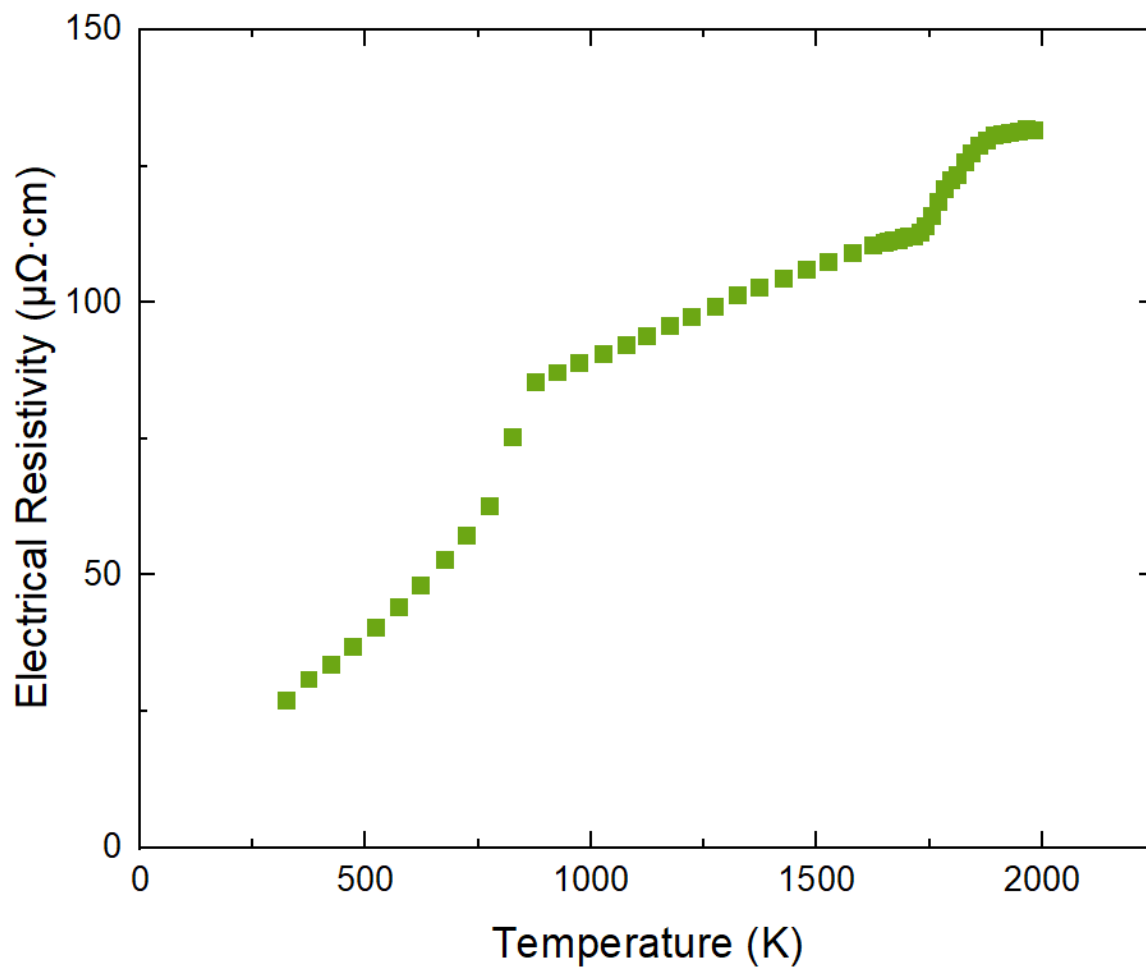
Figure B 7: Electrical resistivity of Fe10Ni at 4 GPa as a function of temperature; data in Table B9

Table B 9: Averaged data from an experimental run (#11) at 4 GPa

Temperature (K)	Voltage (V)	Resistivity (μΩ·cm)	Resistivity (μΩ·cm) corrected for Pt	Thermal Conductivity (W/m/K)
324	0.00088	27.1	27.0	12.6
375	0.00100	30.9	30.8	14.3
423	0.00109	33.5	33.4	15.9
473	0.00120	36.8	36.7	17.6
524	0.00131	40.3	40.2	19.2
575	0.00144	44.2	44.1	20.9
623	0.00156	48.1	48.0	22.5
677	0.00171	52.8	52.6	24.2
725	0.00186	57.3	57.1	25.7
776	0.00204	62.7	62.5	27.4
826	0.00245	75.4	75.2	29.0
878	0.00277	85.4	85.2	30.6
925	0.00283	87.3	87.1	32.1
975	0.00289	89.0	88.8	33.7
1028	0.00295	90.7	90.5	35.3
1078	0.00300	92.3	92.1	36.9
1125	0.00305	93.9	93.7	38.3
1176	0.00311	95.8	95.6	39.8
1223	0.00317	97.6	97.4	41.3
1276	0.00323	99.5	99.2	42.9
1326	0.00330	101.4	101.2	44.4
1374	0.00334	103.0	102.7	45.8
1427	0.00340	104.7	104.4	47.4
1479	0.00345	106.3	106.0	48.9
1526	0.00350	107.8	107.5	50.3
1581	0.00355	109.4	109.1	51.9
1626	0.00360	110.7	110.4	53.3
1652	0.00362	111.3	111.0	54.0
1661	0.00362	111.5	111.2	54.3
1672	0.00363	111.6	111.3	54.6
1682	0.00363	111.8	111.4	54.9
1693	0.00364	112.1	111.7	55.2
1705	0.00365	112.3	111.9	55.5
1717	0.00365	112.5	112.2	55.9
1730	0.00367	113.0	112.7	56.2
1743	0.00371	114.3	114.0	56.6
1756	0.00378	116.3	115.9	57.0
1771	0.00385	118.7	118.3	57.4
1785	0.00393	121.0	120.7	57.8
1799	0.00398	122.6	122.3	58.2
1814	0.00402	123.7	123.4	58.6
1829	0.00409	126.1	125.7	59.1
1844	0.00415	127.8	127.4	59.5
1861	0.00419	129.0	128.6	60.0
1877	0.00423	130.1	129.8	60.4
1895	0.00425	131.0	130.6	60.9
1912	0.00426	131.2	130.8	61.4
1930	0.00427	131.5	131.1	61.9
1947	0.00428	131.7	131.4	62.4
1966	0.00429	132.2	131.8	62.9
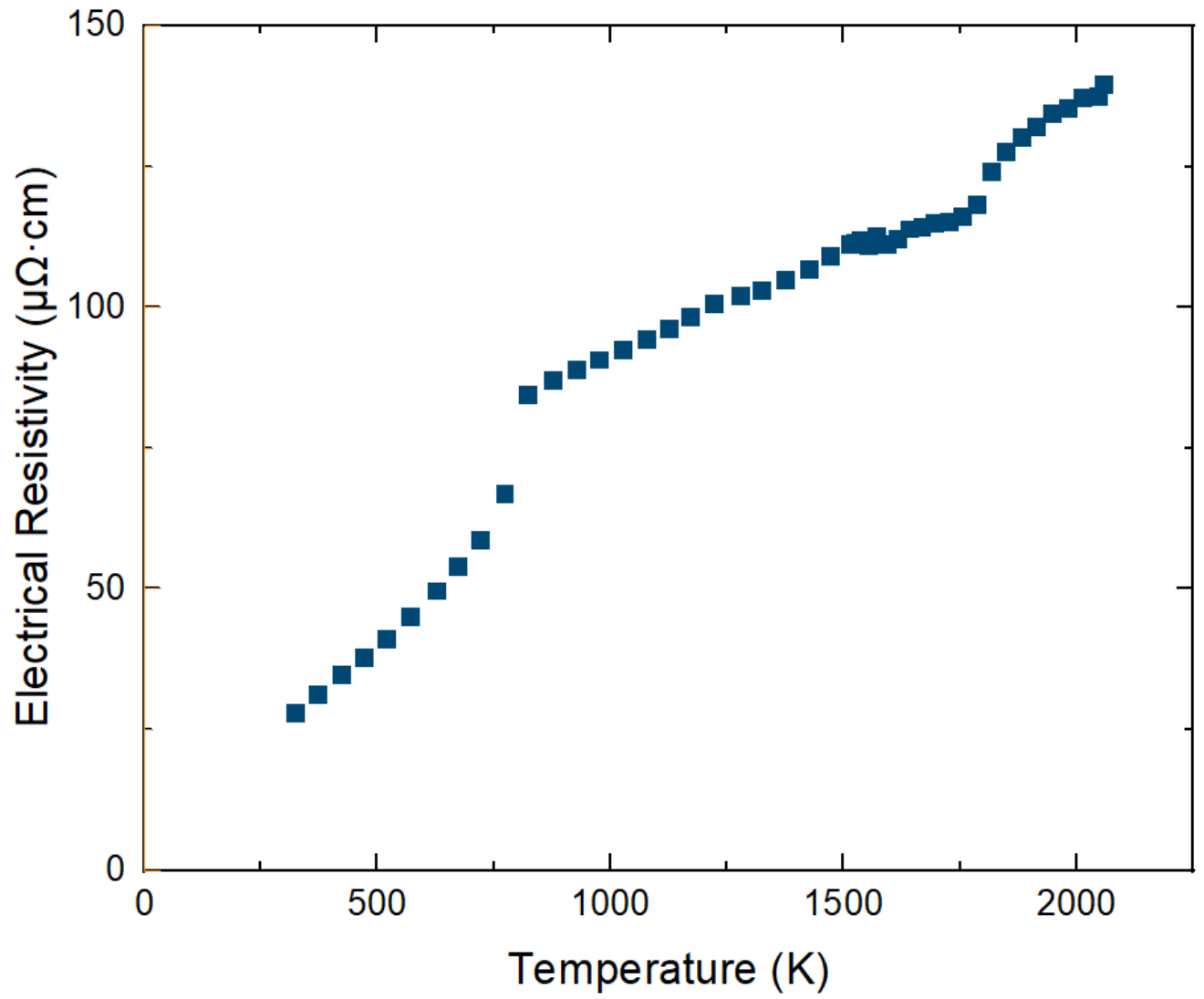
Figure B 8: Electrical resistivity of Fe10Ni at 5 GPa as a function of temperature; data in Table B10

Table B 10: Averaged data from an experimental run (#5) at 5 GPa

Temperature (K)	Voltage (V)	Resistivity (μΩ·cm)	Resistivity (μΩ·cm) corrected for Pt	Thermal Conductivity (W/m/K)
324	0.00092	28.0	28.0	28.3
375	0.00103	31.3	31.2	29.3
426	0.00114	34.7	34.6	30.0
473	0.00124	37.7	37.6	30.7
522	0.00135	41.1	40.9	31.1
573	0.00148	45.1	45.0	31.1
627	0.00163	49.7	49.6	30.9
675	0.00177	54.0	53.9	30.6
723	0.00193	58.7	58.6	30.1
775	0.00220	67.0	66.9	28.3
825	0.00277	84.5	84.3	23.9
878	0.00286	87.0	86.9	24.6
928	0.00292	89.0	88.9	25.5
977	0.00298	90.8	90.6	26.3
1027	0.00304	92.6	92.4	27.1
1078	0.00310	94.4	94.1	27.9
1126	0.00316	96.4	96.2	28.6
1173	0.00323	98.4	98.2	29.2
1225	0.00331	100.8	100.6	29.7
1281	0.00336	102.3	102.1	30.6
1327	0.00339	103.2	103.0	31.4
1376	0.00345	105.0	104.8	32.1
1427	0.00351	107.0	106.7	32.6
1472	0.00359	109.3	109.0	32.9
1516	0.00366	111.4	111.1	33.3
1527	0.00367	111.7	111.4	33.4
1539	0.00368	112.1	111.8	33.6
1554	0.00365	111.1	110.8	34.2
1573	0.00370	112.7	112.4	34.1
1594	0.00366	111.4	111.1	35.0
1618	0.00369	112.5	112.2	35.2
1643	0.00375	114.1	113.8	35.2
1669	0.00376	114.5	114.2	35.7
1698	0.00378	115.1	114.8	36.1
1727	0.00379	115.4	115.1	36.6
1757	0.00382	116.4	116.1	36.9
1787	0.00389	118.5	118.2	36.9
1818	0.00408	124.4	124.1	35.8
1850	0.00419	127.8	127.4	35.4
1883	0.00428	130.4	130.1	35.3
1916	0.00434	132.4	132.0	35.4
1949	0.00442	134.7	134.3	35.4
1982	0.00445	135.7	135.3	35.7
2015	0.00451	137.5	137.1	35.9
2047	0.00452	137.8	137.4	36.3
2060	0.00459	139.9	139.5	36.0

Curriculum Vitae

Name: Eric Lenhart

Post-secondary   Brigham Young University
Education and   Provo, Utah, U.S.A.
Degrees: 2011-2019 B.S.

                                The University of Western Ontario
                                London, Ontario, Canada
                                2019-2021 M.Sc.

Related Work   Teaching Assistant
Experience   The University of Western Ontario
                                2019-2021

Publications: Lenhart, E.M. and Secco, R.A., Implications for the Energy Source for an Early Dynamo in Vesta from Experiments on Electrical Resistivity of Liquid Fe-10wt%Ni at High Pressures, *under review*

                                Lenhart, E.M. and Secco, R.A., Electrical Resistivity of Liquid Fe10wt%Ni at High Pressures and Implications for the Energy Source for an Early Dynamo in Vesta, COMPRES virtual meeting, Aug 12-13, 2021

                                Lenhart, E.M. and Secco, R.A., Electrical Resistivity of Liquid Fe10wt%Ni at High Pressures and Implications for the Energy Source for an Early Dynamo in Vesta, GAC-MAC meeting, virtual and London, ON, Nov 1-5, 2021